

Development and Validation of SAM Multi-dimensional Flow Model for Thermal Mixing and Stratification Modeling

Nuclear Science and Engineering Division

About Argonne National Laboratory

Argonne is a U.S. Department of Energy laboratory managed by UChicago Argonne, LLC under contract DE-AC02-06CH11357. The Laboratory's main facility is outside Chicago, at 9700 South Cass Avenue, Argonne, Illinois 60439. For information about Argonne and its pioneering science and technology programs, see www.anl.gov.

DOCUMENT AVAILABILITY

Online Access: U.S. Department of Energy (DOE) reports produced after 1991 and a growing number of pre-1991 documents are available free at OSTI.GOV (<http://www.osti.gov/>), a service of the US Dept. of Energy's Office of Scientific and Technical Information.

Reports not in digital format may be purchased by the public from the National Technical Information Service (NTIS):

U.S. Department of Commerce
National Technical Information Service
5301 Shawnee Rd
Alexandria, VA 22312
www.ntis.gov
Phone: (800) 553-NTIS (6847) or (703) 605-6000
Fax: (703) 605-6900
Email: orders@ntis.gov

Reports not in digital format are available to DOE and DOE contractors from the Office of Scientific and Technical Information (OSTI):

U.S. Department of Energy
Office of Scientific and Technical Information
P.O. Box 62
Oak Ridge, TN 37831-0062
www.osti.gov
Phone: (865) 576-8401
Fax: (865) 576-5728
Email: reports@osti.gov

Disclaimer

This report was prepared as an account of work sponsored by an agency of the United States Government. Neither the United States Government nor any agency thereof, nor UChicago Argonne, LLC, nor any of their employees or officers, makes any warranty, express or implied, or assumes any legal liability or responsibility for the accuracy, completeness, or usefulness of any information, apparatus, product, or process disclosed, or represents that its use would not infringe privately owned rights. Reference herein to any specific commercial product, process, or service by trade name, trademark, manufacturer, or otherwise, does not necessarily constitute or imply its endorsement, recommendation, or favoring by the United States Government or any agency thereof. The views and opinions of document authors expressed herein do not necessarily state or reflect those of the United States Government or any agency thereof, Argonne National Laboratory, or UChicago Argonne, LLC.

Development and Validation of SAM Multi-dimensional Flow Model for Thermal Mixing and Stratification Modeling

prepared by
Ling Zou, Daniel Nunez, and Rui Hu
Nuclear Science and Engineering Division, Argonne National Laboratory

June 2020

EXECUTIVE SUMMARY

Thermal mixing and stratification in large pools or enclosures are very important phenomena that are critical to nuclear reactor safety. Because of the wide ranges of time and length scales associated with such phenomena, accurate modeling and simulation of thermal mixing and stratification remain as the key unresolved, challenging problems for reactor transient analyses. In traditional system analysis codes, simplified zero-dimensional (0-D) models are widely used for their high numerical efficiency, but they generally suffer from very limited prediction accuracies or range of applicability. Like traditional system analysis codes, the current version of the SAM code has implemented such simplified 0-D and one-dimensional mixing models. On the other hand, high-resolution Computational Fluid Dynamics (CFD) tools are often used to model complex thermal mixing and stratification phenomena. They are, however, generally numerically expensive, and they require large amounts of computational resources. It is therefore desirable to implement advanced and efficient thermal mixing and stratification modeling capabilities embedded in a system analysis code. This approach will improve the accuracy of reactor safety analyses when thermal mixing and stratification are involved, and also avoid using the large computational resources needed for high-resolution CFD analysis.

Currently, with the support of the U.S. DOE Office of Nuclear Energy's Nuclear Energy Advanced Modeling and Simulation program, an effort has been launched to develop and implement a multi-dimensional flow model in the system analysis code SAM, and demonstrate its applications to model thermal mixing and stratification phenomena in large enclosures. The main outcomes of this research and development activity are summarized in this report, which presents an attempt to include a built-in advanced multi-dimensional flow model in a system analysis code with the focus on overcoming the simulation challenges of thermal mixing and stratification phenomena.

In this report, we start with the introduction of existing SAM code capabilities to simulate thermal mixing and stratification phenomena, which is followed by a short summary of the multi-dimensional model implemented in the SAM code, including both the physical model and the Finite Element Method code implementation. In this study, two options were implemented in the SAM code to model turbulent flows: a relatively simple built-in turbulence model and an interface to accept externally computed turbulent viscosities (e.g., from a high-resolution CFD simulation). Code validation studies on this newly added capability were then carried out to compare SAM simulation results with experimental data from the SUPERCAVNA facility, which was designed to study the complex flow recirculation and thermal stratification phenomena relevant to sodium fast reactor designs. In this study, one transient and two steady-state test cases were used for code validation. Different approaches have been used to model the complex turbulence flow fields in the SUPERCAVNA facility. A highly simplified zero-equation turbulence model was first used, but it was determined that it is too simple to capture the complex turbulence flow fields in these test cases. Subsequently, the code validation continued with the use of turbulent viscosity data from high-resolution STAR-CCM+ CFD simulations to improve the accuracy of the results. Using this approach, the SAM simulation results showed very good agreement with both the SUPERCAVNA experimental data and STAR-CCM+ simulation results.

In this report, we demonstrate the development, implementation, and successful validation of a multi-dimensional flow model in the SAM code, which aims to improve the simulation accuracy for complex thermal mixing and stratification phenomena. Lessons have also been learned, including that in cases where the flow fields are not well predicted by the zero-equation model, the input of turbulent viscosities from an external source can enhance the overall predictive capabilities needed to accurately capture complex thermal-hydraulic phenomena. Therefore, future research will be needed to further improve the code's capabilities, such as by developing a more efficient and robust approach to capture the turbulence effects in the SAM code.

TABLE OF CONTENTS

Executive Summary	i
Table of Contents	iii
List of Figures	iv
List of Tables	v
1 Introduction.....	1
1.1 Background.....	1
1.2 SAM 0-D mixing model.....	3
1.3 SAM 1-D mixing model.....	4
1.4 SAM multi-dimensional fluid model	6
2 SAM Multi-dimensional Flow Model.....	8
2.1 Flow equations.....	8
2.1.1 General multi-dimensional flow model.....	8
2.1.2 Porous-medium flow model	10
2.1.3 A unified model	11
2.2 Boundary Conditions.....	12
2.2.1 Inlet	12
2.2.2 Pressure outlet.....	12
2.2.3 Wall	12
2.3 FEM implementation.....	13
2.3.1 Stabilization scheme.....	14
3 Validation of Multi-dimensional Flow Model.....	16
3.1 The SUPERCAVNA facility	16
3.2 Validation cases and computational models.....	17
3.3 Computational models.....	20
4 Code Validation Results	22
4.1 Laminar flow model.....	22
4.2 Zero-equation model	23
4.3 Importing Turbulent Viscosity Distributions.....	24
4.3.1 Transient case T1	25
4.3.2 Steady state cases P3 and P4.....	28
5 Conclusions.....	32
6 Acknowledgment	33
7 References.....	34

LIST OF FIGURES

Figure 1: Multi-volume 0-D pool model.....	3
Figure 2: High-pressure inlet plenum temperature during the BOP-302R test.	4
Figure 3: Outlet temperature response during the postulated loss-of-flow transient.....	6
Figure 4: The framework of data-driven turbulence modeling.....	7
Figure 5: The SUPERCAVNA facility: a) flow directions; b) geometry information and naming convention.	17
Figure 6: Cavity mean inlet temperature for case T1.....	19
Figure 7: a) 2-D representation of the SUPERCAVNA facility; b) Temperature probe locations.....	20
Figure 8: 2-Dimensional mesh of the SUPERCAVNA facility: a) coarse mesh; b) fine mesh.	21
Figure 9: SAM results for case T1: Velocity magnitude distribution.....	22
Figure 10: Typical flow field of a wall bounded jet.	22
Figure 11: Multi-region domain for the zero-equation model. Each color represents a different region.....	23
Figure 12: SAM results for case T1 at $t = 16.7$ mins: a) Velocity distribution; b) Temperature distribution.....	23
Figure 13: Temperature time series for case T1 at the inlet T_{fi} , outlet T_{fa} , and at several y locations (along V2).....	24
Figure 14: CFD results for case T1 at $t = 16.7$ mins: a) Velocity magnitude field; b) Turbulent viscosity field.....	25
Figure 15: CFD results for case T1: Temperature distributions at a) $t = 1.6$ mins; b) $t = 5$ mins; c) $t = 16.7$ mins.	25
Figure 16: CFD results for case T1: Temperature time series at the inlet T_{fi} , outlet T_{fa} , and at several y locations (along V2).....	26
Figure 17: SAM results for case T1: Temperature time series at the inlet T_{fi} , outlet T_{fa} , and at several y locations (along V2).....	27
Figure 18: SAM results for case T1 at $t = 5$ mins: a) Velocity distribution; b) Temperature distribution.....	27
Figure 19: CFD results: Turbulent viscosity distributions for cases a) P3; b) P4.	28
Figure 20: Mesh dependence of the SAM simulations. The arrow points the direction of increasing number of elements.	29
Figure 21: SAM results for case P3: a) Velocity distribution and b) Temperature distribution.	29
Figure 22: SAM results for case P4: a) Velocity distribution and b) Temperature distribution.	30
Figure 23: CFD, SAM, and experimental temperature profiles for cases P3 and P4 at locations: a) V1; b) V2.....	31

LIST OF TABLES

Table 1: SUPERCAVNA facility dimensions.....	17
Table 2: SUPERCAVNA flow conditions.....	19
Table 3: Stainless steel properties.....	19
Table 4: Dimensionless numbers of the test cases.....	20

1 Introduction

1.1 Background

Mixing, thermal-stratification, and mass-transport phenomena in large pools or enclosures play major roles in the safety of reactor systems. Such phenomena include the cold- and hot-pool mixing in pool-type Sodium-cooled Fast Reactors (SFRs), upper plenum or reactor cavity cooling system behavior in High Temperature Gas-cooled Reactors (HTGRs), and thermal stratification in BWR suppression pools. It is very important to accurately predict pool temperature and density distributions for both design optimizations and safety analyses of these reactor systems. The individual transport mechanisms governing mixing are characterized by time and length scales that can span several orders of magnitude. Consequently, large volumes and complex interactions of different flow and thermal structures make the analysis of mixing in a large enclosure a very challenging task. For these reasons, experimental efforts [1–3], including efforts using large facilities like PANDA [3, 4], have been continuously investigating these phenomena over the past three decades. Most recently, the U.S. Department of Energy funded two test facilities [5, 6] through the Nuclear Energy University Program (NEUP), specifically focused on studying thermal stratification phenomena in the upper plenum of SFRs. From a modeling and simulation perspective, depending on the fidelity requirement and computational resources, zero-dimensional (0-D) steady-state models, 0-D lumped-parameter-based transient models, one-dimensional (1-D) physics-based models, and three-dimensional (3-D) Computational Fluid Dynamics (CFD) models are all available. A good overview of major modeling methods for thermal mixing and stratification phenomena and their advantages and limits is presented by Zhao and Peterson [7].

With respect to system analysis tools, the capability of current major system-analysis or severe-accident-analysis codes (such as SAS4A/SASSYS-1 [8], RELAP5-3D [9], CATHRE [10], and MELCOR [11]) is quite limited. They either have no models or only 0-D models for thermal mixing and stratification in large enclosures. The lack of general thermal mixing and stratification models in those codes limits their application and accuracy for safety analysis for conditions in which thermal stratification plays an important role, especially for reactors relying on natural circulation for long-term cooling.

For example, the SAS4A/SASSYS-1 code developed by Argonne National Laboratory (Argonne), one of the major SFR system analysis codes, provides lumped-volume-based 0-D models that can give very approximate results and can only handle simple cases with one mixing source. The models were derived according to simulant experiments for specific SFR upper-plenum design configurations. Depending on the momentum and buoyancy of the outlet flow from the reactor core, a well-mixed case, a two-zone case with a negative buoyant jet, a two-zone case with a positive buoyant jet, and even more complex three-zone cases may form. The total jet entrainment, zone interface location, and average temperatures in each zone can be estimated by empirical correlations. Since the methods are based on scaled experimental data, using those models for SFR designs with different hot/cold-pool configurations tends to result in large uncertainties.

Note that a multi-dimensional component is available in RELAP5-3D and TRACE, and can be used to define a 3-D array of volumes and the internal junctions connecting the volumes. However, for both RELAP5-3D and TRACE, the 3-D components are designed primarily for reactor vessel (i.e., core, downcomer) and steam generator applications. These reactor

components have solid structures in the fluid path (i.e., core, steam generator) or have a short length in the radial direction (i.e., downcomer) that causes the form loss, wall friction, and interphase friction models to be the primary source terms in the momentum equations. For these applications, the viscous stress and turbulence terms are not as important and are not included in the 3-D models. Since these terms are not present in the codes, the RELAP5-3D and TRACE 3D models should not be used to model large open tanks.

Scaling analyses for the prediction of thermal stratification and mixing in pools and in large interconnected enclosures were developed and applied by Peterson and coworkers at UC Berkeley [12, 13]. A 1-D simulation code, BMIX/BMIX++, was also developed to simulate stratification development under stably stratified conditions [14]. The ambient fluid volume is represented by 1-D transient partial differential equations (PDEs), and substructures such as free or wall jets are modeled with 1-D integral models. This allows very large reductions in computational effort compared to 3-D CFD modeling. This simulation code was validated against a number of benchmark problems [15, 16]; however, BMIX++ cannot model the transition cases where the fully stratified ambient or well-mixed ambient assumptions break down. For a transient where an initially stratified pool is gradually mixed, it cannot help to infer the time scale for such mixing processes. Two recent efforts have been made to develop 1-D models for thermal stratification with the support of the two NEUP projects, one by Wilson and Bindra [17] and the other by Lu et al. [18]. However, the two approaches have similar limitations to the work from UC Berkeley, as mentioned above.

Reynolds-Averaged Navier-Stokes (RANS)-based CFD approaches are less expensive than higher fidelity Large Eddy Simulations (LES), and have been applied in SFR upper-plenum simulations with very detailed geometric modeling of major structures [19]. However, it is still computationally overwhelming to perform long-transient unsteady RANS (uRANS)-based CFD simulations in engineering applications for complex flow conditions, particularly when sensitivity/uncertainty analysis is needed for design optimizations and safety analyses. Multi-scale modeling approaches (achieved by coupling 1-D system and 3-D CFD codes) have been used to simulate large and complex domains by modeling the large volume with a CFD code and the rest of the system with a system code [20]. This methodology can provide detailed information only where needed, while providing system-level information in the rest of the domain. However, coupling different codes employing different solver routines and operating at different spatial and temporal scales remains a challenge. A notable fundamental problem is that a reliable and accurate coupling scheme is largely missing in the treatment of momentum and energy exchange at the boundary between the CFD model and the system model.

It is very desirable to have an advanced and efficient thermal mixing and stratification modeling capability embedded in a system analysis code to improve the accuracy of reactor safety analyses and to reduce modeling uncertainties. An advanced system analysis tool, SAM [21], is under development at Argonne for advanced non-LWR reactor safety analysis. It aims to provide fast-running, modest-fidelity, whole-plant transient analyses capabilities, which are essential for fast-turnaround design scoping and engineering analyses of advanced reactor concepts. While SAM is being developed as a system-level modeling and simulation tool [22, 23], advanced modeling techniques, including a reduced-order 3-D module, are under development to tackle the issue of thermal mixing and stratification modeling in large enclosures of reactor systems during transients.

This report discusses recent developments concerning the reduced-order flow modeling capabilities in SAM for thermal stratification and mixing. Three different modeling approaches have been pursued. The first one is similar to the approach used in conventional system codes, which models a large enclosure with multiple 0-D volumes. The second approach is based on 1-D fluid models, with additional terms accounting for the thermal mixing from both macroscopic flow circulations and microscopic turbulent mixing. The third approach is based on a 3-D coarse-grid CFD approach, in which the multi-dimensional fluid conservation equations are modeled with closure models to account for the effects of turbulence. The technical basis, progress, and limitations of the three modeling approaches are discussed in Section 1. Section 2 covers the governing equations, models, and implementations in the SAM multi-dimensional flow model. Section 3 introduces the code validation cases, and Section 4 presents the code validation results.

1.2 SAM 0-D mixing model

A general multiple 0-D volume modeling approach like that used in conventional system codes is also implemented in SAM, as shown in Figure 1. A large enclosure is modeled by a number of 0-D averaged volumes, where inter-volume directional flow and mixing flows are allowed.

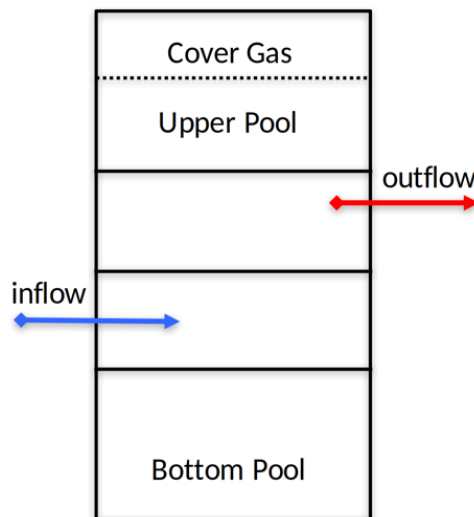


Figure 1: Multi-volume 0-D pool model.

The feasibility of the multiple 0-D volume modeling approach in SAM was tested using an available EBR-II loss-of-heat-sink test (BOP-302R), where the intermediate sodium pump was tripped without scrambling the control rods or tripping the primary pumps. This test was driven by increasing core inlet temperatures, which were a result of the diminished IHX heat rejection due to the lower intermediate sodium flow rates. Strong thermal stratification is expected in the primary vessel (cold pool), where the IHX outlet and the pump inlets are located in the upper part of the vessel.

In the SAM BOP-302R simulation, the mixing flow between the upper and lower cold pool is assumed to be 50% of the primary core flow rate. The comparisons of high-pressure inlet plena temperatures from the SAM simulation and the test results are shown in Figure 2. Very

good agreement was achieved between the SAM simulation and the test results for both the initial heat-up rates and the later pseudo-equilibrium states. More details on the SAM model and simulation results can be found in an earlier paper [24]. It was demonstrated that the thermal stratification in the cold pool during the test can be modeled with a relatively simple multiple 0-D volume model. Note that the mixing flow rates between 0-D volumes are crucial to accurately model the heat transfer between 0-D volumes, and the mixing flow rates could be derived from uRANS-based CFD simulations. To check the validity of this assumption, the uRANS-based CFD simulation results were used to derive the mixing flow rates throughout the whole transient. However, it was found that the mixing flow rate was not constant throughout the transient, and the magnitude was much higher than the 50% of normal core flow rate during most of the transient. This finding indicates that the assumption of a constant mixing flow rate used in the SAM simulation of the BOP-302 test is not valid, even though the simulation results matched well with the experimental results. Further studies would be needed to develop correlations between the mixing flow rates at horizontal cross planes and the lumped sub-volume parameters.

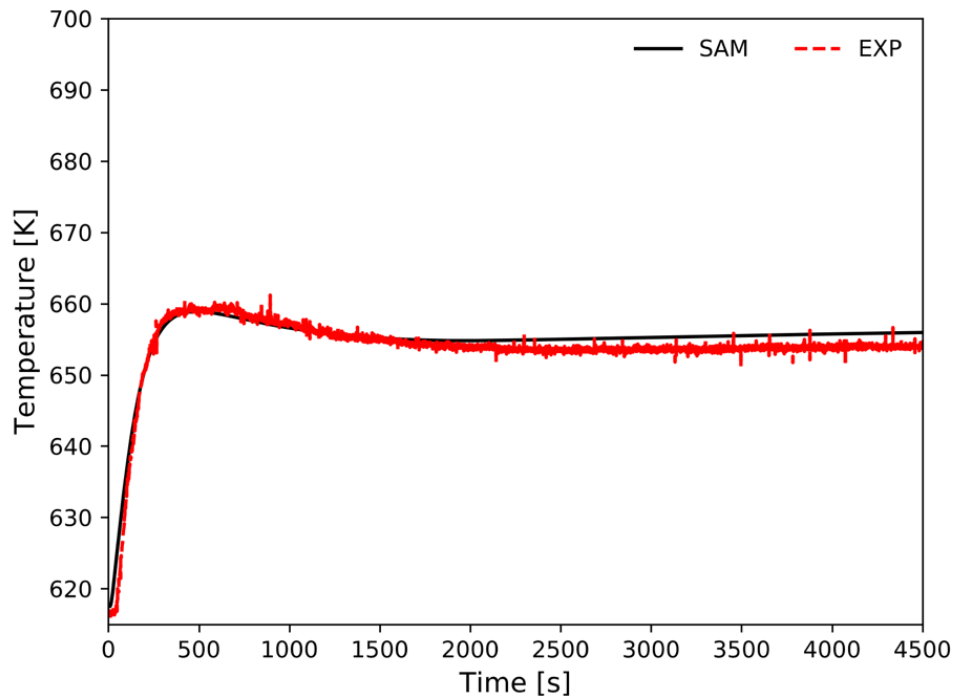


Figure 2: High-pressure inlet plenum temperature during the BOP-302R test.

1.3 SAM 1-D mixing model

The SAM 1-D modeling approach is similar to the SAM multiple 0-D volume approach, where the large enclosure can be divided into an arbitrary number of sub-volumes, separated by horizontal interfaces. The inter-volume energy exchange can be modeled by both advection and flow mixing. The 1-D fluid conservation equations are used for the 1-D axial mixing model. To consider the flow mixing, the energy conservation equation can be written as

$$\frac{\partial(\rho H)}{\partial t} + \frac{\partial[(\rho u + G_{mix})H]}{\partial z} = \nabla(k\nabla T) \quad (1)$$

where ρ is the density; H the enthalpy; u the 1-D average flow velocity; $G_{mix} = \rho u_m$ the mixing mass flux, in which u_m is the mixing flow velocity; k the thermal conductivity; and T the temperature. Note that additional models for the mixing mass flux are needed, for which the high-fidelity CFD simulations using LES and uRANS can assist in the closure model development.

An additional governing equation (Equation 2) is introduced for the mixing flow velocity. Note that its form is not originated from momentum conservation, but derived on the basis of the energy conservation equation. The left side of the equation is the transport part (time derivative and advection terms), while the right side includes the diffusion term, resistance term, and the source terms. Recognizing three major contributions of the mixing flow, i.e., local flow velocity, geometry, and buoyancy effects, two parameters, C_{gb} and C_{gv} , are introduced in the mixing-velocity equation:

$$\frac{\partial \rho u_m}{\partial t} + \frac{\partial(\rho u u_m)}{\partial z} = \mu \nabla^2 u_m + \frac{c_f f}{2D} \rho u_m^2 + C_{gb} \beta \rho g \nabla T - \frac{c_f f}{2D} \rho (C_{gv} u)^2 \quad (2)$$

where μ is the dynamic viscosity, f the friction coefficient using the average flow velocity u and the equivalent hydraulic diameter D , c_f the multiplier of the friction coefficient, β the thermal expansion coefficient of the fluid, C_{gb} the coefficient for the buoyancy effects in the specific geometry (with a default value of 1 if its value is not provided by the users), and C_{gv} the coefficient for the velocity effects in the specific geometry (with a default value of the area ratio between the tank cross-section area and the inlet pipe area).

To verify the applicability of the developed 1-D axial mixing model, a stand-alone tank test problem was simulated with the 1-D model. Transient CFD simulations of the stand-alone tank model are used as the reference solutions. The tank outlet temperature responses during the transient are shown in Figure 3 for various modeling approaches. With increasing complexity of the model, the SAM simulation results became closer to the reference CFD simulation results. For some cases, the upper part of the tank (above the outlet pipe) was neglected in the models. Consequently, the outlet temperature responses were far away from the reference CFD simulation results. From the CFD simulation results, it is clear that the upper part was not stagnant and strongly participated in the flow circulation and mixing in the tank. Once the upper tank is modeled, the 1-D simulation results are much closer to the CFD results. This preliminary demonstration case provides us with some confidence that the 1-D axial mixing model could simulate the macroscopic tank behavior during the transient with both accuracy and efficiency. The details of this study are given by Hu et al. [25].

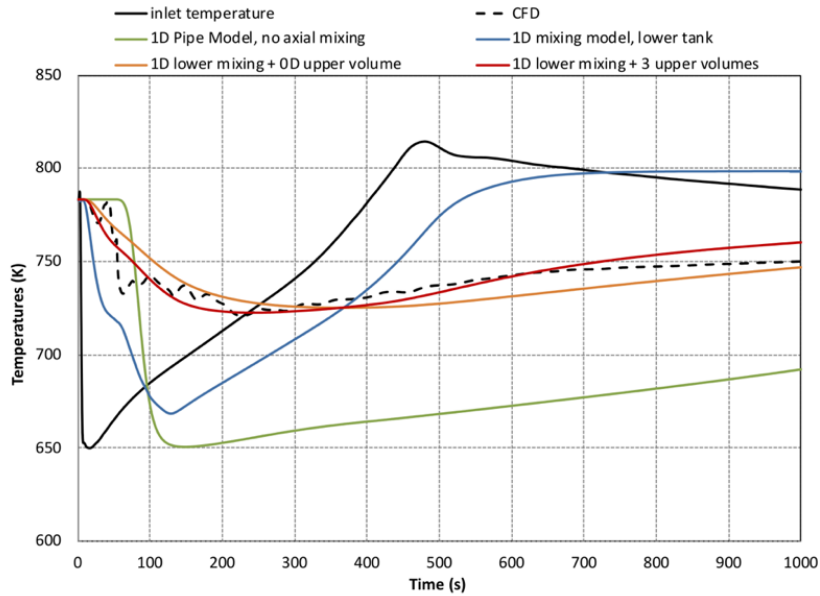


Figure 3: Outlet temperature response during the postulated loss-of-flow transient.

1.4 SAM multi-dimensional fluid model

A reduced-order 3-D flow module is also under development in SAM to tackle the issue of thermal mixing and stratification modeling in large enclosures of reactor systems during transients. The main objective of the SAM 3-D fluid model is to provide a computationally efficient modeling capability to model the multi-dimensional flow and thermal stratification phenomena in large enclosures in nuclear systems. To achieve this objective, the key modeling approaches include the following:

- Solving the full 3-D fluid equation;
- Using only coarse computational meshes;
- Performing no turbulence modeling;
- Developing closure models to account for the effects of turbulence and the use of coarse meshes in momentum and energy transport.

The framework of a 3-D Finite Element Method (FEM) flow model has been developed and implemented in SAM. To prevent potential numerical instability issues, the Streamline-Upwind/Petrov-Galerkin (SUPG) and the Pressure-Stabilizing/Petrov-Galerkin (PSPG) formulations have been implemented. Several verification and validation tests were performed, including lid-driven cavity flow, natural convection inside a cavity, and laminar flow in a channel of parallel plates. On the basis of the comparisons between the analytical solutions and experimental results, it is demonstrated that the developed 3-D fluid model can perform very well for a range of laminar flow problems. Very good agreements were found between SAM simulation results and the experimental results. More details on the SAM 3-D fluid model and the initial verification and validation results can be found in an earlier paper [26].

Continued efforts are required on closure-model development based on high-fidelity CFD simulation results. Note that a data-driven turbulence model approach is also being pursued via an Argonne LDRD project to leverage machine learning techniques to establish a surrogate model in SAM to replace the turbulence model in traditional CFD codes. The data-driven

modeling approach has received increasing interest in the research community, including preliminary research on nuclear thermal fluid applications. The framework of the data-driven turbulence modeling approach, which consists of four steps, is depicted in Figure 4.

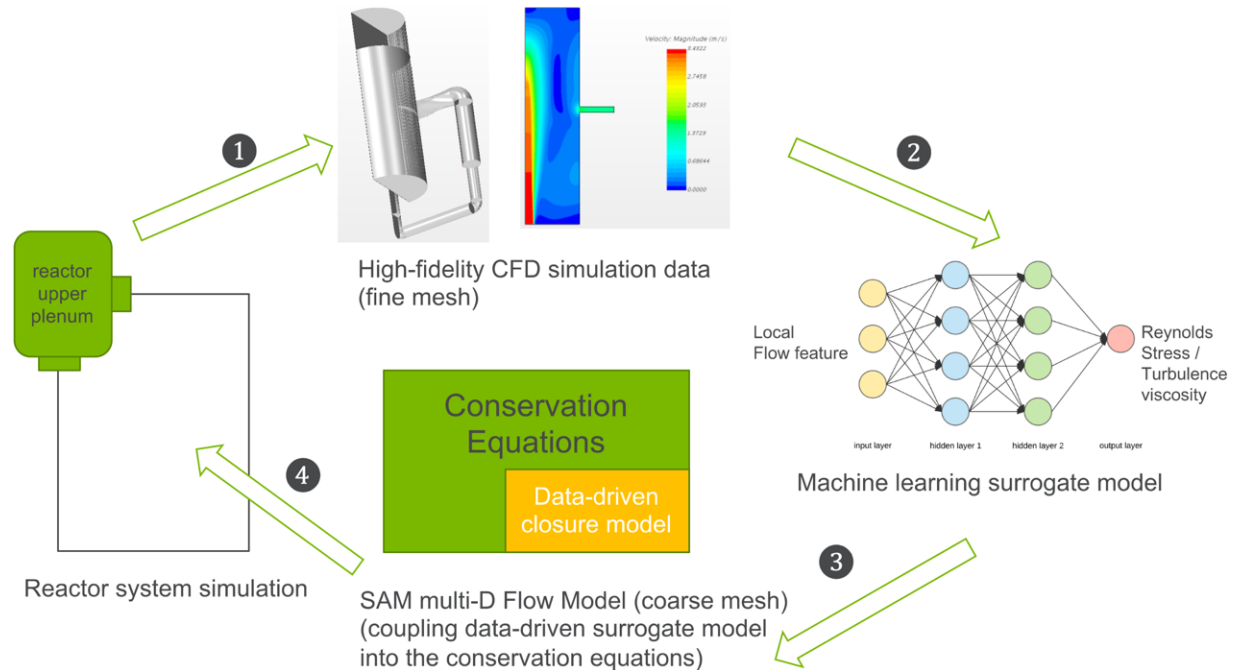


Figure 4: The framework of data-driven turbulence modeling.

2 SAM Multi-dimensional Flow Model

In SAM, a unified multi-dimensional flow model has been developed and implemented to consider both the general multi-dimensional flow model and the porous medium-based flow model. In this chapter, we will discuss the governing equations, types of boundary conditions, and code implementation of the SAM multi-dimensional model.

2.1 Flow equations

In this section, we will start with the general multi-dimensional flow model in Subsection 2.1.1, followed by a discussion of the porous-medium flow model in Subsection 2.1.2. A unified flow model based on these two flow models will be discussed in Subsection 2.1.3.

2.1.1 General multi-dimensional flow model

For the general multi-dimensional flow model, the set of balance equations for fluid flow in three dimensions includes the mass, momentum, and energy balance equations:

$$\frac{\partial \rho}{\partial t} + \nabla \cdot (\rho \mathbf{V}) = 0, \quad (3)$$

$$\rho \frac{\partial \mathbf{V}}{\partial t} + \rho (\mathbf{V} \cdot \nabla) \mathbf{V} + \nabla p - \rho \mathbf{g} - \nabla \cdot \boldsymbol{\tau} = 0, \quad (4)$$

$$\rho c_p \frac{\partial T}{\partial t} + \rho c_p \mathbf{V} \cdot \nabla T - \nabla \cdot (k \nabla T) - q''' = 0, \quad (5)$$

where $\mathbf{V} = [V_x, V_y, V_z]^T$ is the velocity vector. The convection term in the momentum equation, i.e., $\rho (\mathbf{V} \cdot \nabla) \mathbf{V}$, can be explicitly expressed as

$$\rho (\mathbf{V} \cdot \nabla) \mathbf{V} = \begin{bmatrix} \rho \mathbf{V} \cdot \nabla V_x \\ \rho \mathbf{V} \cdot \nabla V_y \\ \rho \mathbf{V} \cdot \nabla V_z \end{bmatrix}. \quad (6)$$

If compressibility effects are considered, following [27], the viscous tensor, $\boldsymbol{\tau}$, can be expressed as

$$\boldsymbol{\tau} = \mu \left[\nabla \mathbf{V} + (\nabla \mathbf{V})^T - \frac{2}{3} (\nabla \cdot \mathbf{V}) \mathbf{I} \right], \quad (7)$$

and therefore,

$$\nabla \cdot \boldsymbol{\tau} = \mu \nabla^2 \mathbf{V} + \frac{1}{3} \mu \nabla (\nabla \cdot \mathbf{V}), \quad (8)$$

where $\nabla \mathbf{V}$ is a second-order tensor with $[\nabla \mathbf{V}]_{ij} = \partial V_i / \partial x_j$, for $i, j = x, y, z$; and \mathbf{I} is the identity tensor. The Laplacian term, $\mu \nabla^2 \mathbf{V}$, is defined as

$$\mu \nabla^2 \mathbf{V} = \mu \nabla \cdot (\nabla \mathbf{V}) = \mu \begin{bmatrix} \nabla^2 V_x \\ \nabla^2 V_y \\ \nabla^2 V_z \end{bmatrix}. \quad (9)$$

It is clear that the divergence term, $\nabla \cdot \mathbf{V}$, is non-zero for compressible flows where the fluid density depends on pressure, or for thermally expandable flows where the fluid density depends on temperature. Typically, this term only contributes to negligible effects for low-speed flow conditions. For applications of interest to SAM simulations, which typically do not involve highly compressible flow conditions, it is reasonable to ignore this term, and thus,

$$\nabla \cdot \boldsymbol{\tau} = \mu \nabla^2 \mathbf{V}. \quad (10)$$

With this equality, the momentum equation (4) can be written as

$$\rho \frac{\partial \mathbf{V}}{\partial t} + \rho (\mathbf{V} \cdot \nabla) \mathbf{V} + \nabla p - \rho \mathbf{g} - \mu \nabla^2 \mathbf{V} = 0. \quad (11)$$

Although it is not our intention to develop SAM as a CFD tool, turbulence effects must be considered to obtain physically plausible and numerically stable solutions. There are several turbulence models available, ranging from the very simple zero-equation models to the more complex and widely used two-equation models (i.e., $k - \varepsilon$ and $k - \omega$), and even more complex turbulence models with more equations. Zero-equation models are easy to implement and computationally less expensive; however, they generally can only be applied under very simple flow conditions. More complex turbulence models, such as the $k - \varepsilon$ and $k - \omega$ models, are more attractive options because of their larger validation domains; however, these models are more computationally expensive, and therefore, are not considered in the current SAM development.

Nevertheless, when turbulence effects are considered, the molecular viscosity μ is replaced with the effective viscosity μ_{eff} . The effective viscosity includes the contributions from both the molecular-viscosity and turbulent-viscosity effects, i.e.,

$$\mu_{eff} = \mu + \mu_t, \quad (12)$$

where μ_t is the turbulent viscosity. Furthermore, the effects of turbulent flow on heat dissipation in the energy equation also need to be considered. In a similar manner, the fluid thermal conductivity k is replaced with an effective value, i.e.,

$$k_{eff} = k + k_t, \quad (13)$$

where k_t is the enhanced thermal conductivity due to turbulence effects, and is related to the turbulent viscosity by

$$k_t = \frac{c_p \mu_t}{Pr_t}, \quad (14)$$

where c_p is the specific heat and Pr_t the turbulent Prandtl number. While different values for k_{eff} have been reported by various resources (e.g., 0.85 by FLUENT), in this study we use the default value of 0.9 as reported by Yoder [28].

Currently, SAM provides two options to represent the turbulent viscosity. The first option is a simple zero-equation model implemented in SAM that computes the turbulent viscosity on the basis of Prandtl's mixing-length theory [29]:

$$\mu_t = \rho L_{mix}^2 \sqrt{2 \sum_{i,j=1}^{i,j=3} S_{ij} S_{ij}}, \quad (15)$$

where $S_{ij} = \mathbf{S} = \frac{1}{2} [\nabla \mathbf{V} + (\nabla \mathbf{V})^T]$ is the rate-of-strain tensor. It is noted that more complex zero-equation models exist, which consider wall effects (e.g., the Cebeci-Smith and Baldwin-Lomax models) [30]; however, these models were not implemented. Moreover, the second option in SAM allows the user to import the turbulent viscosity from an external source. These turbulent-viscosity distributions can be obtained from high-resolution CFD simulations or from machine learning models.

2.1.2 Porous-medium flow model

To address the modeling and simulation needs of pebble-bed reactors such as high-temperature gas-cooled or fluoride-salt-cooled reactors, a porous-medium-based multi-dimensional flow model (porous-medium flow model) has recently been implemented in the SAM code. In nuclear reactor thermal-hydraulic analyses, it is a common approach to utilize porous-medium flows to model the fluid flow and heat transfer in very complex geometries, such as the pebble-bed cores and tube bundles in steam generators. This subsection provides a brief discussion of the porous-medium flow model currently implemented in SAM.

For the porous-medium flow model, we follow the models presented in [31] with some necessary extensions. The complete set of balance equations includes the mass, momentum, and energy equations for the fluid phase, as well as the energy equation for the solid phase.

$$\epsilon \frac{\partial \rho}{\partial t} + \nabla \cdot (\rho \mathbf{v}) = 0, \quad (16)$$

$$\rho \frac{\partial \mathbf{v}}{\partial t} + \frac{\rho}{\epsilon} (\mathbf{v} \cdot \nabla) \mathbf{v} + \epsilon \nabla p - \epsilon \rho \mathbf{g} + \alpha \mathbf{v} + \beta |\mathbf{v}| \mathbf{v} = 0, \quad (17)$$

$$\epsilon \rho c_p \frac{\partial T}{\partial t} + \rho c_p \mathbf{v} \cdot \nabla T - \nabla \cdot (\epsilon k \nabla T) - q''' + a_w h (T - T_s) = 0, \quad (18)$$

$$(1 - \epsilon) \rho_s c_{p,s} \frac{\partial T_s}{\partial t} - \nabla \cdot (k_{s,eff} \nabla T_s) - q_s''' + a_w h (T_s - T) = 0, \quad (19)$$

where subscript s denotes the solid phase, ϵ is the porosity of the pebble bed, and \mathbf{v} is the so-called superficial velocity, which is related to the intrinsic velocity \mathbf{V} by $\mathbf{v} = \epsilon \mathbf{V}$. For the mass balance equation (Equation 16), we follow the same Equation 1.1 presented in [31]. For the momentum equation, we use Equation 1.8 from [31] as the basic model, and extend the drag term to include both the linear viscous (Darcy) and quadratic (Forchheimer) terms. Other higher-order partial-derivative terms, such as the Brinkman term analogous to the Laplacian term in the Navier-Stokes equation, are not included. For fluid and solid energy equations, we follow Equations 2.2 and 2.1 of [31], respectively. It is noted that, for the diffusion term of the fluid energy equation, the porosity ϵ is moved into the divergence, which seems more

appropriate if local averaged fluid thermal conductivity is assumed to be ϵk (see discussion in Section 3.2.1 of [32]). Nevertheless, the contribution of this conduction term to energy transport is normally trivial compared to the convection term, especially under convection-dominant conditions. It is also noted that, for the diffusion term of the solid energy equation, instead of using the simple form of $(1-\epsilon)\nabla\cdot(k_s\nabla T_s)$ given in [31], we use $\nabla\cdot(k_{s,eff}\nabla T_s)$, which is a more sophisticated approach and requires an additional closure correlation to model $k_{s,eff}$, the effective thermal conductivity of porous media. The last term in both the fluid-flow energy and solid-phase energy equations are the convective heat transfer term, in which a_w is the heating surface area density per unit volume, and h is the heat transfer coefficient.

2.1.3 A unified model

As clearly shown in the previous two subsections, the general multi-dimensional fluid flow model and the porous-medium flow model have many similarities. In many applications, there is also a need to include both flow models in the same simulations. For example, in simulations of HTGR core multi-dimensional flows, it is typical to model flows in both the top and bottom plena using the general multi-dimensional flow model and flow through the pebble-bed core using the porous-medium approach. Therefore, a unified model based on these two sets of flow equations has been developed to reduce the effort of code implementation, as well as to ease the model input process when both flow models are needed in the same simulation.

For the unified flow model, the fluid mass, momentum, and energy balance equations are given as follows:

$$\epsilon \frac{\partial \rho}{\partial t} + \nabla \cdot (\rho \mathbf{v}) = 0, \quad (20)$$

$$\rho \frac{\partial \mathbf{v}}{\partial t} + \frac{\rho}{\epsilon} (\mathbf{v} \cdot \nabla) \mathbf{v} + \epsilon \nabla p - \epsilon \rho \mathbf{g} + \mathbf{F}_m = 0, \quad (21)$$

$$\epsilon \rho c_p \frac{\partial T}{\partial t} + \rho c_p \mathbf{v} \cdot \nabla T - \nabla \cdot (\epsilon k \nabla T) - q''' + S_e = 0 \quad (22)$$

The source term, \mathbf{F}_m , in the momentum equation is given as

$$\mathbf{F}_m = \begin{cases} -\mu \nabla^2 \mathbf{V} & (general\ model) \\ \alpha \mathbf{v} + \beta |\mathbf{v}| \mathbf{v} & (porous - medium\ model) \end{cases} \quad (23)$$

and the additional source term in the energy equation, S_e , in the fluid energy equation is given as

$$S_e = \begin{cases} 0 & (general\ model) \\ a_w h (T - T_s) & (porous - medium\ model) \end{cases} \quad (24)$$

It is noted that, if $\epsilon = 1$, this model exactly reduces to the general multi-dimensional flow model given in Section 2.1.1. For the simulation of a porous medium, where the solid structure is also modeled, the same solid-phase energy equation, Equation (19), is used.

2.2 Boundary conditions

In this section, the physical boundary conditions are discussed. Their mathematical form and implementation within the FEM will be discussed in the coming sections. We will concern ourselves with a limited set of boundary conditions of engineering interest to SAM simulations, and by no means do we intend to list all possibilities. This limited set of boundary conditions is discussed in the following subsections.

2.2.1 Inlet

For an inlet flow condition, the magnitude of the inlet velocity $|\mathbf{v}_{in}|$ and inlet temperature T_{in} are to be specified. Both parameters could be constant values, or functions of time and/or position. With a given inlet velocity magnitude, local density computed from pressure (as part of the solution), and temperature (from boundary conditions), the inlet mass flux can then be computed. The three velocity components for the inlet flow will also be specified for the momentum equations, and obviously they have to be consistent with the specified value for the magnitude of inlet velocity.

2.2.2 Pressure outlet

For an outlet flow condition, it is typical to specify the outlet pressure p_{out} , which could be a constant value or a function of time and/or position. No fluid temperature should be given unless a reverse flow condition is expected on part of or on the entire outlet boundary during a transient, which, if possible, should be avoided by moving the pressure outlet further downstream. In addition, it is generally acceptable to deem the viscous effects unimportant, and to allow them to be ignored at the pressure outlet boundary. The same argument could be directly applied to the energy equation, such that the effect of the diffusion term on the boundary is ignored.¹

2.2.3 Wall

For solid walls, we apply a non-penetrating condition, such that the mass flux normal to the wall is zero. For the energy equation, several different boundary conditions could be applied. The simplest one to apply is a Dirichlet type of boundary condition for the fluid temperature. A Neumann type of boundary condition can also be applied, in which a wall heat flux is required. An adiabatic condition is a special Neumann boundary condition, where the temperature gradient is zero. For the momentum equation, two types of boundary conditions are considered:

¹ First, in the context of incompressible flows, an outlet boundary condition is generally a different concept than a prescribed pressure boundary condition. An outlet boundary condition is normally ascribed to an outlet that is far in the downstream direction, where the gradients of all variables (except pressure) are zero [33]. In general, it is not necessarily true that the velocity gradients will be zero on a prescribed pressure boundary. However, it is generally safe to assume that those gradients are zero on the “transparent” outlet boundary for the advection-diffusion equation [34, 35], and it was found that the smaller the viscosity, the smaller the introduced error [35]. The momentum equation is indeed an advection-diffusion equation, and the viscosity, which is the kinematic viscosity for the momentum equation, is generally very small. A similar argument could be made for the energy equation. To the energy equation, the thermal diffusivity is analogous to the kinematic viscosity in the momentum equation. Thermal diffusivities of typical fluids of interest to our simulations are also generally very small, and therefore it is acceptable to use the “transparent” boundary condition as well.

- Non-slip wall
All velocity components are simply set to zero.
- Slip wall
Viscous effects at the wall can be neglected (viscous stress-free boundary). It is noted that a rigorous implementation of generic slip-wall boundary conditions on a wall, using an arbitrary geometry, is not a trivial task [36–38]. A viscous stress-free boundary is really an engineering simplification, and users should be cautious of the potential inaccuracies that could arise from such a simplification.

2.3 FEM implementation

As a MOOSE-based application, SAM uses a FEM to obtain the discretized equations, which are then solved with the Jacobian-free Newton-Krylov (JFNK) method provided by the MOOSE framework. Instead of directly solving the PDEs, SAM solves the so-called “weak form” of the PDEs. Using FEM, the weak forms of the discretized equations are obtained by multiplying the governing equations by a test function, ψ , and then integrating over the domain. Here, we use the mass balance equation (Equation 20) as an example to introduce several FEM concepts. By using integration by parts and applying the Divergence Theorem, we obtain the weak form for the mass balance equation as

$$\begin{aligned} & \int_{\Omega} \psi \left[\epsilon \frac{\partial \rho}{\partial t} + \nabla \cdot (\rho \mathbf{v}) \right] d\Omega \\ & = \int_{\Omega} \psi \epsilon \frac{\partial \rho}{\partial t} d\Omega + \int_{\partial\Omega} \psi \rho \mathbf{v} \cdot \hat{\mathbf{n}} d\Gamma - \int_{\Omega} \nabla \psi \cdot \rho \mathbf{v} d\Omega = 0 , \end{aligned} \quad (25)$$

where Ω is the domain of interest (i.e., volume), $\partial\Omega$ is the boundary of the domain (i.e., boundary surface), and $\hat{\mathbf{n}}$ is the outward-pointing unit normal of the boundary surfaces. In the context of FEM, it is common to use $(,)$ to denote a volume integral, and \langle , \rangle to denote a surface integral. It is also typical to write the discretized equations in the residual form when the JFNK method is used.

Using the FEM notations, the residual forms of the unified multi-dimensional flow equations are given as follows:

$$\mathbf{r}'_c = \left(\epsilon \frac{\partial \rho}{\partial t}, \psi \right) + (-\rho \mathbf{v}, \nabla \psi) + \langle \rho \mathbf{v} \cdot \hat{\mathbf{n}}, \psi \rangle \quad (26)$$

$$\mathbf{r}'_m = \left(\rho \frac{\partial \mathbf{v}}{\partial t}, \psi \right) + \left(\frac{\rho}{\epsilon} (\mathbf{v} \cdot \nabla) \vec{u}, \psi \right) + (\epsilon \nabla p, \psi) + (-\epsilon \rho g, \psi) + F_m \quad (27)$$

$$\begin{aligned} \mathbf{r}'_e = & \left(\epsilon \rho c_p \frac{\partial T}{\partial t}, \psi \right) + (\rho c_p \mathbf{v} \cdot \nabla T, \psi) + (\epsilon k \nabla T, \nabla \psi) + \langle -\epsilon k \nabla T \cdot \hat{\mathbf{n}}, \psi \rangle \\ & + (-q''' + S_e, \psi) \end{aligned} \quad (28)$$

and the residual form of the solid-phase energy equation (if applicable) is given as

$$r_s = \left((1 - \epsilon)\rho_s c_{p,s} \frac{\partial T_s}{\partial t}, \psi \right) + (k_{s,eff} \nabla T_s, \nabla \psi) + \langle -k_{s,eff} \nabla T_s \cdot \hat{n}, \psi \rangle + (-q''' + S_e, \psi) \quad (29)$$

In the residual equations discussed above, the superscript “'''” indicates that they are not in their final forms, as additional stabilization terms will be added (see next section). The subscripts c , m , e , and s denote the mass balance (continuity), momentum, fluid flow energy, and solid-phase energy equations, respectively.

The source term in its weak form, F_m , in the residual form of the momentum equation is

$$F_m = \begin{cases} (\mu \nabla \mathbf{v}, \nabla \psi) + \langle -\mu \nabla \mathbf{v} \cdot \hat{n}, \psi \rangle & (\text{general model}) \\ (\alpha \mathbf{v} + \beta |\mathbf{v}| \mathbf{v}, \psi) & (\text{porous - medium model}) \end{cases} \quad (30)$$

2.3.1 Stabilization scheme

It is well understood that stabilization schemes are necessary for the standard Continuous Galerkin FEM to regulate spurious spatial numerical oscillations, when it is applied to convection-dominant problems. In SAM, the SUPG and PSPG schemes are both implemented to resolve numerical instability issues. Both schemes introduce additional terms into the original weak form of the balance equations. For the mass balance equation, an additional PSPG term is added:

$$r_c = r'_c + (R_m, \tau_{PSPG} \nabla \psi), \quad (31)$$

and for the momentum and energy equations, an additional SUPG term is added for each equation:

$$r_m = r'_m + (R_m, \tau_{SUPG,m} \mathbf{v} \cdot \nabla \psi) \quad (32)$$

$$r_e = r'_e + (R_e, \tau_{SUPG,e} \mathbf{v} \cdot \nabla \psi), \quad (33)$$

where R_m and R_e are the raw residual forms of the momentum and the energy equation, respectively. These equations are the original PDEs without being multiplied by the test function or integrated by parts, i.e.,

$$R_m = \rho \frac{\partial \mathbf{v}}{\partial t} + \frac{\rho}{\epsilon} (\mathbf{v} \cdot \nabla) \mathbf{v} + \epsilon \nabla p - \epsilon \rho \mathbf{g} + F_m, \quad (34)$$

and

$$R_e = \epsilon \rho c_p \frac{\partial T}{\partial t} + \rho c_p \mathbf{v} \cdot \nabla T - \nabla \cdot (\epsilon k \nabla T) - q''' + S_e. \quad (35)$$

The stabilization parameters are given as

$$\tau_{PSPG} = \left[\left(\frac{2}{\Delta t} \right)^2 + \left(\frac{2V}{h} \right)^2 + \left(\frac{4v}{h^2} \right)^2 \right]^{-1/2} \quad (36)$$

$$\tau_{SUPG,m} = \left[\left(\frac{2}{\Delta t} \right)^2 + \left(\frac{2|\mathbf{v}|}{h} \right)^2 + \left(\frac{4v}{h^2} \right)^2 \right]^{-1/2} \quad (37)$$

and

$$\tau_{SUPG,e} = \left[\left(\frac{2}{\Delta t} \right)^2 + \left(\frac{2|\mathbf{v}|}{h} \right)^2 + \left(\frac{4\alpha}{h^2} \right)^2 \right]^{-1/2}, \quad (38)$$

where V is a reference velocity magnitude, which, if not provided, is by default the local velocity magnitude $|\mathbf{v}|$; ν the kinematic viscosity; α the thermal diffusivity; Δt the time-step size; and h the local mesh size (normally taken as the smallest edge length of the local mesh element). For more details on the PSPG/SUPG theory, implementation, and additional references, we refer the reader to [26]. It is also noted that the solid-phase energy equation (Equation 19) for the original PDE, and Equation (29) for its weak form, do not require stabilization schemes, as they are simply heat conduction equations.

3 Validation of Multi-dimensional Flow Model

Three verification and validation test cases have been studied to evaluate the laminar flow modelling capabilities of the SAM multi-dimensional flow model. The test cases are the lid-driven cavity flow, the laminar flow in a channel of parallel plates, and the natural convection inside a square cavity. The consistency between the code simulations and analytical solutions or experimental data indicates that SAM can provide efficient and accurate simulation of the laminar flow by the embedded multi-dimensional flow model, as discussed in [26]. Using the recently updated multi-dimensional model, similar results were obtained for the three simple laminar-flow test cases, which are not elaborated in this report.

To validate SAM's multi-dimensional flow model for more complex flow with turbulence mixing and thermal-stratification phenomena, experimental data obtained in the SUPERCARVNA facility are utilized. In this section, we will describe the experimental facility, the data used for validation, and the computational models used.

3.1 The SUPERCARVNA facility

The SUPERCARVNA facility at the French Alternative Energies and Atomic Energy Commission (CEA) was designed to study liquid sodium flows relevant to SFRs, including flow recirculation and thermal stratification [39, 40]. Formation and destruction of thermal stratification can occur under certain flow conditions in the upper plenum of SFRs. This facility consists of a stainless-steel rectangular cavity with inlet and outlet channels at the bottom of the cavity. The cavity's right wall can be heated through a secondary sodium loop (heating channel), while all the other walls are thermally insulated. Once liquid sodium is injected into the cavity, a wall-bounded jet develops and spreads in the vertical direction. Part of this jet exits the cavity through the outlet channel, while the rest impinges on the right wall and creates a recirculation region. This region varies in size depending on the rate of sodium injection at the inlet and the strength of the thermally stratified layers (layers with different temperatures) created at the top of the tank as a result of the temperature gradient imposed by the heating channel. The facility, flow directions, and naming conventions used throughout this report are illustrated in Figure 5. The facility's dimensions are provided in Table 1.

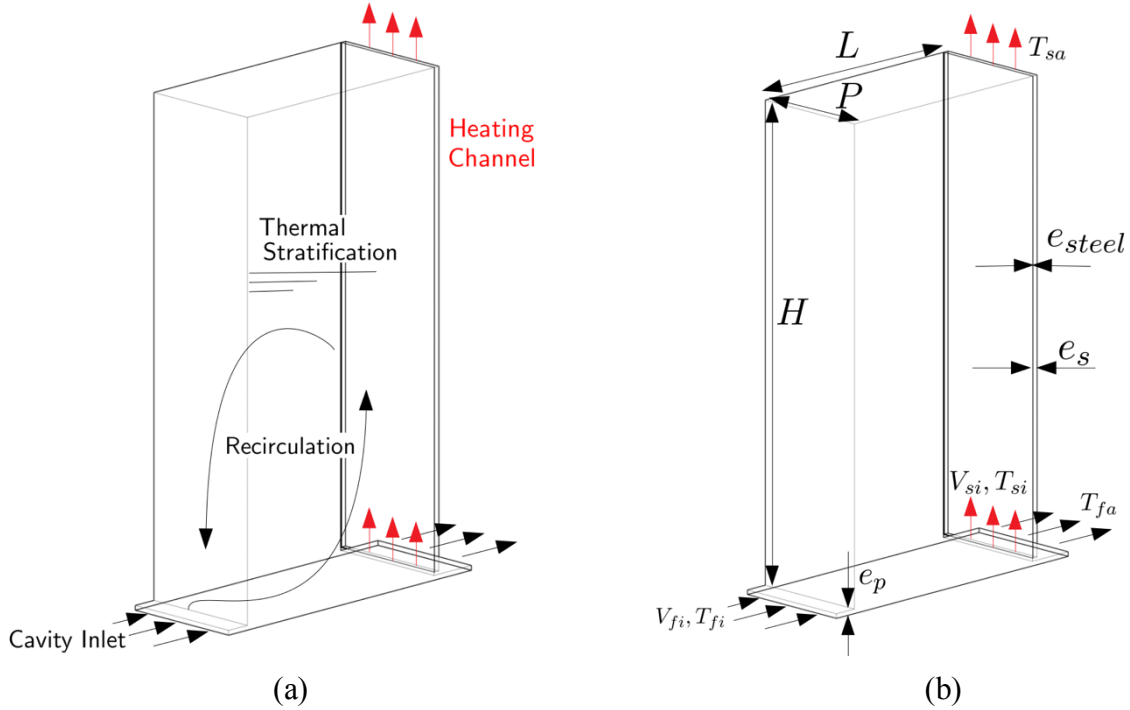


Figure 5: The SUPERCAVNA facility: a) flow directions; b) geometry information and naming conventions.

Table 1: SUPERCAVNA facility dimensions.

Parameter	Symbol	Value (m)	Parameter/L
Height	H	3.2	2
Length	L	1.6	1
Depth	P	0.8	0.5
Cavity inlet and outlet thickness	e_p	0.0304	0.019
Heating channel inlet and outlet thickness	e_s	0.035	0.21875
Stainless steel thickness	e_{steel}	0.006	0.00375

3.2 Validation Cases

Three experimental data sets were utilized to validate SAM's multi-dimensional flow model: one transient case and two steady-state cases. The steady-state cases consist of flows with a strong buoyancy presence induced by the heating channel. In these cases, the cavity is initially filled with liquid sodium with temperature T_0 . Then, sodium with the same constant temperature is injected into the cavity at a constant flow rate. Simultaneously, sodium at a higher constant temperature is injected into the heating channel, and heats up the cavity throughout the transient. Consequently, a region of thermally stratified layers of sodium, of

increasing temperatures along the height of the tank, are formed and eventually reach a steady state.

The transient case, on the other hand, consists of a forced-convection experiment, where liquid sodium is injected at a constant flow rate with decreasing temperatures, as shown in Figure 6. For this case, the heating channel is not in use, and therefore, the right wall acts as an adiabatic boundary. A summary of the initial and boundary conditions for the steady-state and transient cases is provided in Table 2. Moreover, the stainless-steel material properties are essentially constant for the temperature range of interest; therefore, the constant values provided in Table 3 were used. Finally, the temperature-dependent sodium material properties were utilized using the built-in sodium property models in SAM.

The following list provides further details about the boundary conditions implemented in the models:

- A fully developed velocity profile is imposed at the inlet of the cavity and heating channel.
- A pressure outlet is imposed at the outlet of the cavity and heating channel.
- The conjugate heat transfer between the cavity and the stainless steel, and between the stainless steel and the heating channel, are directly resolved in simulations.
- Non-slip boundary conditions are set at the walls.
- All walls are adiabatic with the exception of the walls with solid-fluid contacts.

Furthermore, the flow regimes for these experiments were characterized by the Reynolds (Re), Prandtl (Pr), Peclet (Pe), and Richardson (Ri) numbers as defined in [39]. These dimensionless numbers were calculated on the basis of the initial inlet conditions in the cavity using the following expressions:

$$Re = \rho V_{fi} L_0 / \mu, \quad (39)$$

$$Pr = c_p \mu / k, \quad (40)$$

$$Pe = Re Pr = \rho c_p V_{fi} L_0 / k, \quad (41)$$

$$Ri = g \beta \Delta T L_0 / V_{fi}^2, \quad (42)$$

where ρ is the density, V_{fi} the cavity mean inlet velocity, L_0 the characteristic length scale (chosen to be the cavity's length L), μ the dynamic viscosity, c_p the specific heat, k the thermal conductivity, g the acceleration due to gravity, and β the volumetric thermal expansion coefficient.² Furthermore, for the transient case, ΔT corresponds to the temperature drop at the inlet channel (i.e., $\Delta T = T_{fi}(t_0) - T_{fi}(t_f)$), while for the steady-state cases, ΔT corresponds to the difference between the maximum temperature and the inlet temperature in the cavity (i.e., $\Delta T = T_{c2} - T_{fi}$).

The dimensionless numbers for the three cases are provided in Table 4. The case with the highest Reynolds number and lowest Richardson number corresponds to the forced convection case T1, while the case with the lowest Reynolds number and highest Richardson number corresponds to the most buoyancy-dominant case, P4.

² A value of $\beta = 2.26 \times 10^{-4} \text{ K}^{-1}$ is used, in accordance with [41].

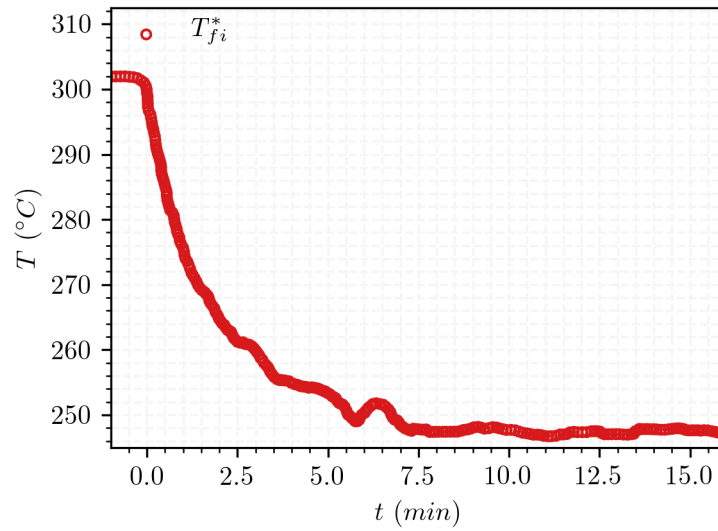


Figure 6: Cavity mean inlet temperature for case T1.

Table 2: SUPERCAVNA flow conditions.

Parameter	Symbol	Unit	Case P3	Case P4	Case T1
Maximum temperature in the cavity	T_{c2}	°C	294.4	296.6	302
Global initial temperature	T_0	°C	250	250	302
Cavity mean inlet velocity	V_{fi}	m/s	0.69	0.3	1.27
Cavity mean inlet temperature	T_{fi}	°C	250	250	See Figure 6
Heating channel mean inlet velocity	V_{si}	m/s	0.69	0.3	N/A
Heating channel mean inlet temperature	T_{si}	°C	303.1	303.1	N/A

Table 3: Stainless steel properties.

Parameter	Symbol	Unit	Value
Density	ρ	kg/m ³	8000
Thermal conductivity	k	W/(m-K)	18
Specific heat capacity	c_p	J/(kg-K)	480

Table 4: Dimensionless numbers of the test cases.

Case	Re	Pr	Pe	Ri
T1	5.28×10^6	5.59×10^{-3}	2.95×10^4	1.14×10^{-1}
P3	2.52×10^6	6.25×10^{-3}	1.58×10^4	3.31×10^{-1}
P4	1.10×10^6	6.25×10^{-3}	0.69×10^4	1.84×10^0

3.3 Computational models

The cavity's inlet thickness is approximately 2 orders of magnitude smaller than its length (i.e., $e_p/L = 0.019$). This wide range in dimensions leads to a wide range of flow length scales, which makes this a challenging and computationally expensive problem to model. In order to reduce the computational costs without sacrificing the accuracy of the model, we take advantage of the symmetry of the facility and create a 2-D domain. The CAD geometry along with the meshes presented in this report were created using the Salome platform's CAD modeler and mesher [42]. The model is separated into three regions: a cavity (fluid), a stainless-steel wall (solid), and a heating channel (fluid). These regions, as well as the location of the origin axis, are shown in Figure 7a. The locations of the experimental measurement probes are shown in Figure 7b. Here, $\tilde{y} = y/L$ is the location along the height of the cavity scaled by its length.

Furthermore, the 2-D domain was discretized using quadrangles. While the objective of the multi-dimensional flow model is to use coarse meshes to improve the computational efficiency of the simulations, mesh convergence studies were carried out to ensure mesh independence. Coarse to fine meshes, as shown in Figure 8, were used for the simulations described in Section 4.

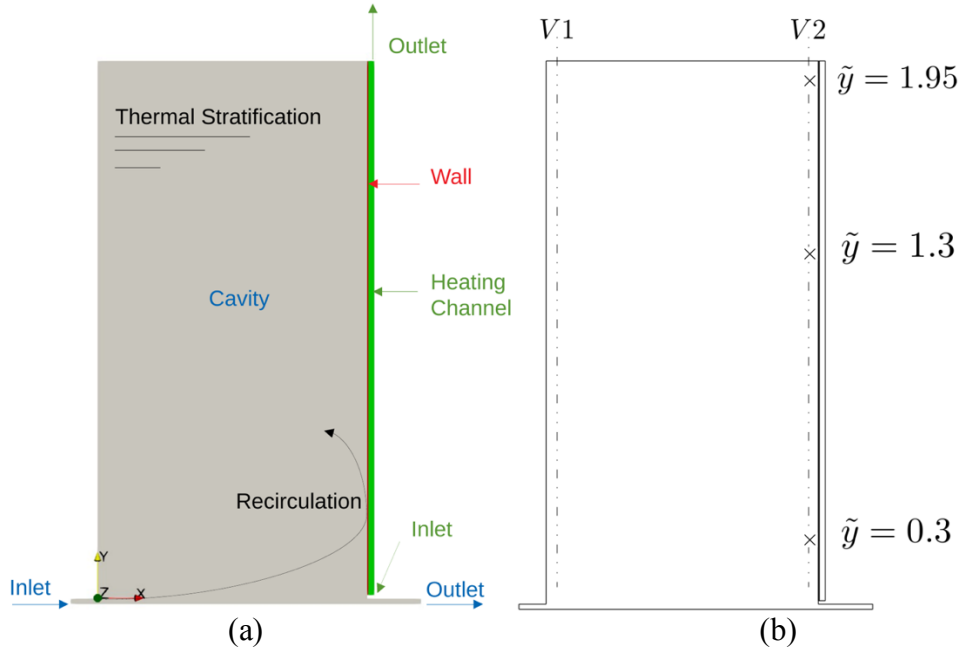


Figure 7: a) 2-D representation of the SUPERCAVNA facility; b) temperature probe locations.

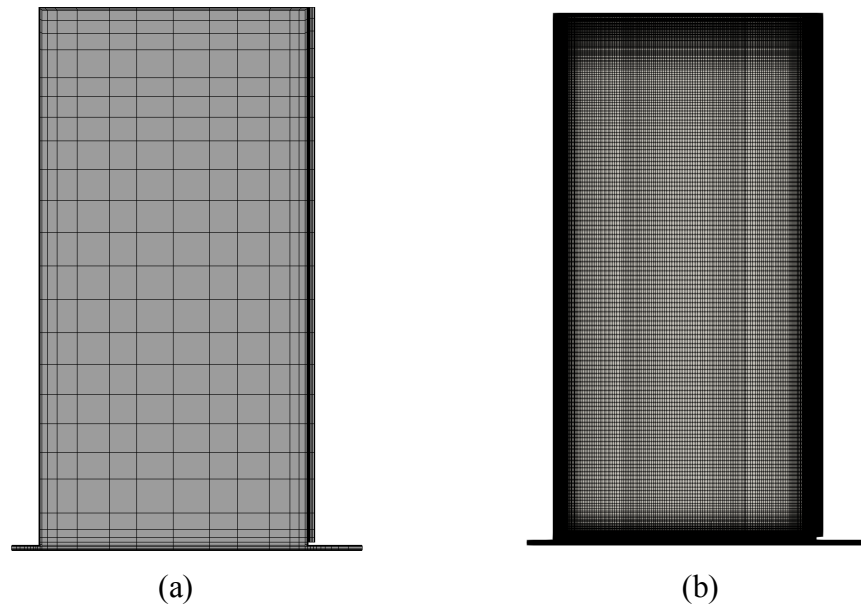


Figure 8: 2-Dimensional mesh of the SUPERCANVA facility: a) coarse mesh; b) fine mesh.

As mentioned in Subsection 2.1.1, to represent the turbulence field, we can use a zero-equation model, or import the turbulent viscosity field from CFD simulations or surrogate machine learning models. In Section 4, we provide the results obtained with both approaches. The imported turbulent viscosity was obtained from RANS and uRANS CFD simulations using the commercial code STAR-CCM+ [43]. We would like to note that it is not our intention to provide complete details about the CFD simulations. This CFD model is mainly used as a reference tool to estimate how well the flow fields can be predicted through CFD, and to obtain the turbulent viscosity for the SAM simulations. The following list contains the models selected in STAR-CCM+³:

- Two-Dimensional, Liquid, Gradients, Gravity
- Steady-state solver (cases P3, P4), Implicit unsteady solver (case T1)
- Segregated flow
- Segregated fluid temperature
- User-defined equations of state (the same as the sodium property models in SAM)
- Constant turbulent Prandtl number⁴ $Pr_t = 0.9$
- Two-layer All y^+ treatment
- Realizable $k - \epsilon$ turbulence model, two-layer with the buoyancy-driven (Xu) formulation

³ The default coefficients for these models were used.

⁴ The same implementation and value are used in the SAM multi-dimensional model.

4 Code Validation Results

As mentioned above, prior to this work, a model capable of performing well for laminar flows was implemented in SAM. In this section, we first discuss why the laminar formulation is unable to predict the high-Reynolds-number flow field encountered in the SUPERCAVNA facility. Then, we demonstrate how the inclusion of turbulence information leads to improved predictions of the flow fields of the validation cases (i.e., flow recirculation and thermal stratification).

4.1 Laminar-flow model

The velocity magnitude distribution for the transient case T1, obtained with a SAM simulation using the laminar formulation, is shown in Figure 9. In the inlet channel, the flow field exhibits typical characteristics seen in channel flows; however, once this flow enters the cavity, unexpected flow behaviors are encountered. Given that the flow entering the cavity encounters a wall on one side and an open volume of fluid on the other side, wall-bounded jet-flow characteristics are expected. As shown in Figure 10, a typical wall-bounded jet flow exhibits a decay of its centerline velocity and an expansion of the shear layers on the side of open volume. Using the laminar formulation, the aforementioned flow characteristics are not captured. Instead, the incoming flow continues its trajectory towards the outlet without jet expansion, and as a result, the jet does not create a recirculation region. Consequently, inaccurate prediction of the temperatures across the cavity are obtained. In Sections 4.2 and 4.3, we describe how the unified flow model is able to provide improved flow predictions.

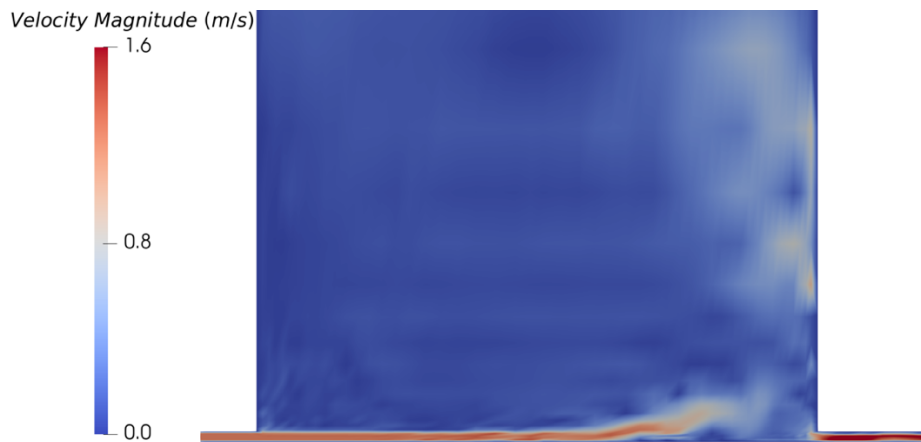


Figure 9: SAM results for case T1: Velocity magnitude distribution.



Figure 10: Typical flow field of a wall-bounded jet.

4.2 Zero-equation model

As described in Section 2.1.1, the zero-equation model is known to perform well only for simple flows. In this section, the abilities of the zero-equation model to predict the flow field for case T1 are discussed. In this model, the computation of the turbulent viscosity depends on mixing length L_{mix} (see Equation 15), which varies between different regions of the computational domain. Consequently, the user is given the option to define a single mixing length for the complete domain, or various values for different regions as needed. For example, three different mixing lengths can be prescribed for the three regions shown in Figure 11. The mean velocity and temperature distributions obtained by defining three mixing lengths are shown in Figure 12. In this case, the jet's shear layers spread slightly more, and as a result, a recirculation region is created in the bottom part of the cavity. Consequently, the temperature distribution exhibits a lower temperature only in that region.

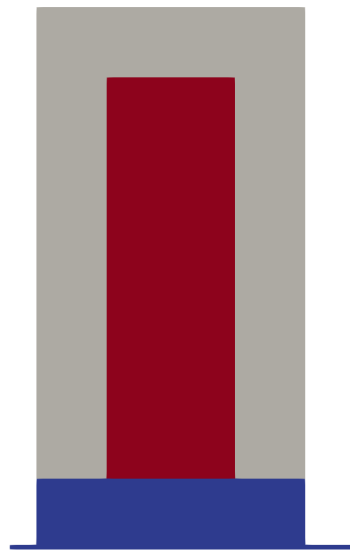


Figure 11: Multi-region domain for the zero-equation model. Each color represents a different region.

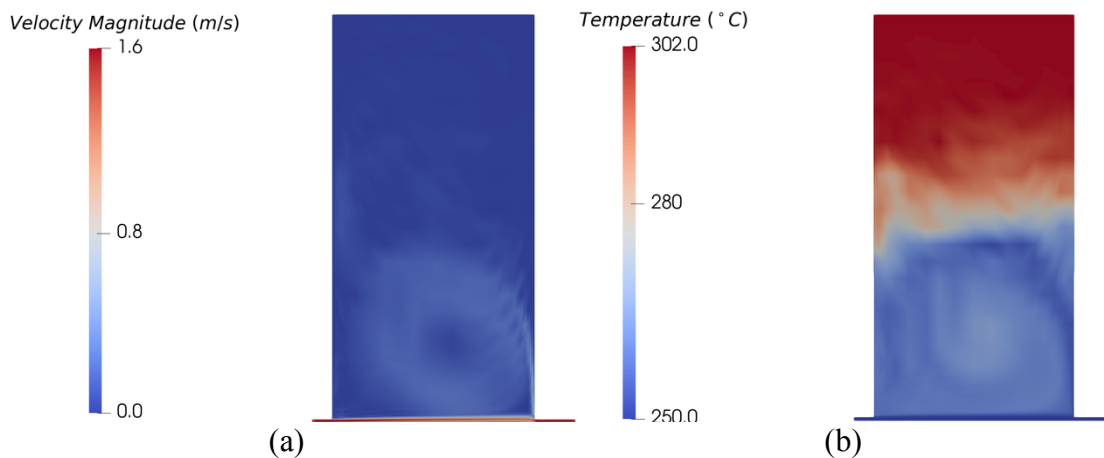


Figure 12: SAM results for case T1 at $t = 16.7$ min: a) Velocity distribution; b) temperature distribution.

A comparison between the experimental data and SAM results for the temperature time series at the cavity’s outlet, and at several \tilde{y} locations (along V2), is provided in Figure 13. We would like to note that the experimental time series for the different \tilde{y} locations were indistinguishable. Consequently, two bounding curves (in gray), which encloses the range of the data for these three locations, was created.

In this validation case, the temperature in the lower region of the cavity ($\tilde{y} = 0.3$) falls within the expected range of the experimental data during the first 10 minutes of the transient, until it starts overpredicting the temperature. Since the recirculation region is limited to the lower half of the cavity, the temperatures at $\tilde{y} = 1.30, 1.95$ are completely overpredicted by SAM. Consequently, owing to the small mixing region of the colder incoming fluid with the warmer fluid in the upper region of the cavity, the outlet temperature is underpredicted through most of the transient.

While defining three regions with different mixing lengths helped improve the model to predict a recirculation region, this model is unable to capture the whole flow field without significantly increasing the number of fluid regions. On the basis of these results, the zero-equation approach was considered as an inappropriate option for this validation case.

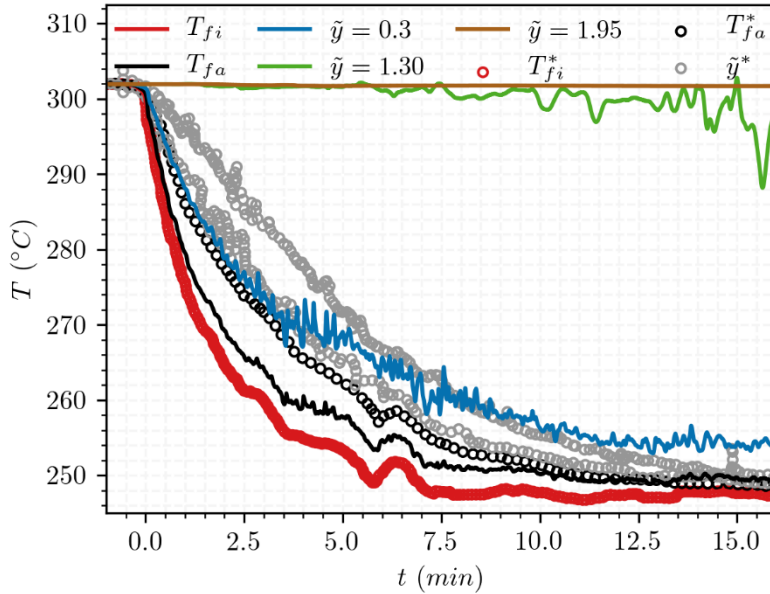


Figure 13: Temperature time series for case T1 at the inlet T_{fi} , outlet T_{fa} , and several \tilde{y} locations (along V2). The circles and solid lines represent the experimental data and the SAM results, respectively. Note that T_{fi} is overlapping with T_{fi}^* .

4.3 Importing Turbulent-viscosity Distributions

In this section, we will evaluate the SAM unified flow model with a user-provided turbulent-viscosity distribution as an input. The discussions for the transient and steady-state validation cases are provided in Sections 4.3.1 and 4.3.2, respectively.

4.3.1 Transient case T1

To obtain the turbulent viscosity distribution for this validation case, a CFD simulation using STAR-CCM+ was performed. The velocity magnitude, turbulent viscosity, and temperature distributions, shown in Figure 14 and Figure 15, exhibit a large recirculation region in the center of the cavity. This pattern indicates that the flow travels from the bottom of the right wall to the top of the cavity and creates a large vortex as the fluid travels to the other walls in a counterclockwise direction. Additionally, the temperature distributions at different times during the transient, shown in Figure 15, further illustrate the large recirculation area created by the colder incoming fluid.

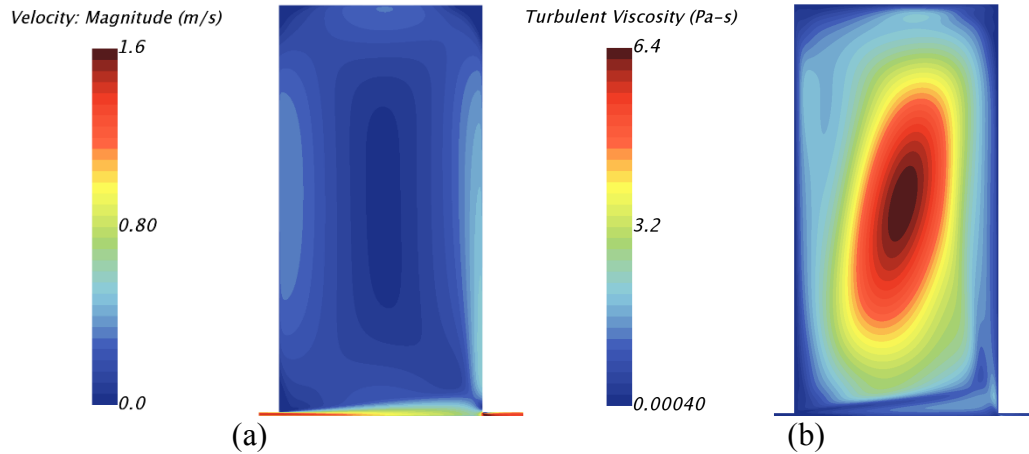


Figure 14: CFD results for case T1 at $t = 16.7$ mins: a) Velocity-magnitude field; b) turbulent-viscosity field.

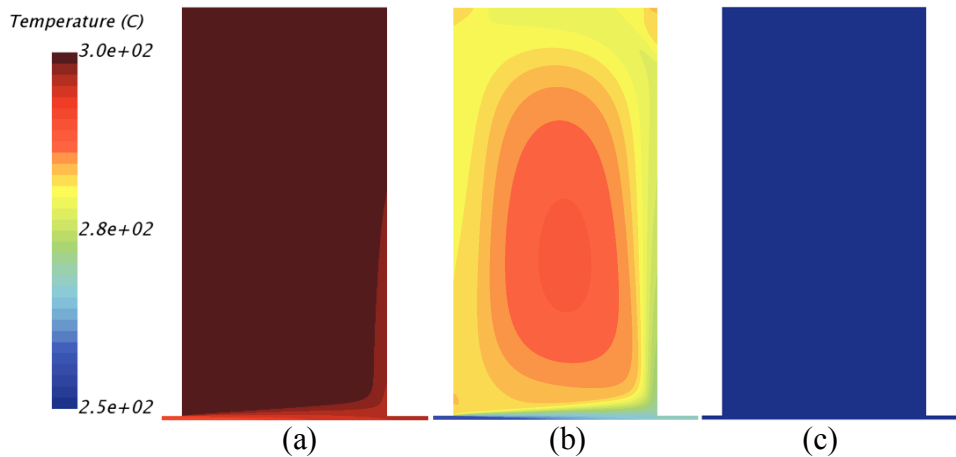


Figure 15: CFD results for case T1: Temperature distributions at a) $t = 1.6$ mins; b) $t = 5$ mins; c) $t = 16.7$ mins.

Furthermore, a comparison of the temperature time series at the inlet, outlet, and several \tilde{y} locations (along V2) is provided in Figure 16. The time series at the different \tilde{y} locations are well predicted by the CFD model. Time series for $\tilde{y} = 0.30, 1.30$ fall within the expected temperature range; however, at $\tilde{y} = 1.95$ (near the top of the cavity), the differences between the experimental data and CFD results can be as large as 2°C . Since the temperatures at the different heights of the cavity are generally well predicted, the outlet temperature is well predicted also.

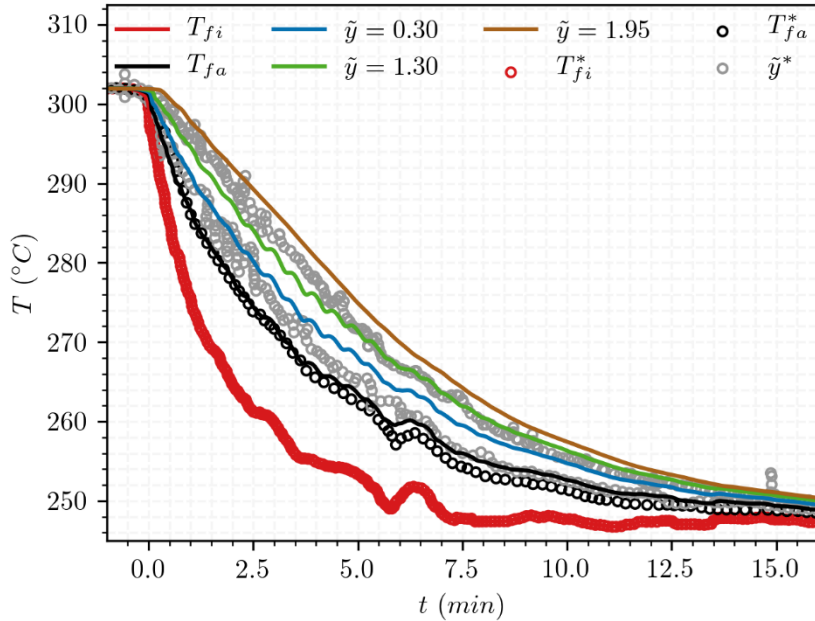


Figure 16: CFD results for case T1: Temperature time series at the inlet T_{fi} , outlet T_{fa} , and several \tilde{y} locations (along V2). The circles and solid lines represent the experimental data and the CFD results, respectively. Note that T_{fi} is overlapping with T_{fi}^* .

While the recirculation area in the CFD simulation varies throughout the transient, these variations are small; therefore, a pseudo-steady-state turbulent viscosity is used as the SAM input file, and therefore the CFD-predicted turbulent viscosity data were imported into SAM only once at the beginning of the simulation. This minimizes the cost associated with data transferring and data mapping, because of different meshes used in CFD and SAM simulations. However, for simulations where the turbulent viscosity profile significantly changes with time, a time-dependent turbulent viscosity profile will have to be imported. With this imported turbulent viscosity option, we are able to obtain better flow predictions without the implementation of turbulence models. The time series obtained with SAM are shown in Figure 17. The time series at heights $\tilde{y} = 0.3$ and 1.30 are very well predicted. On the other hand, at $\tilde{y} = 1.95$, large differences arise during the first 10 min of the transient. These discrepancies can be explained by inspecting the velocity and temperature distributions.

The distributions at time $t = 5$ min, shown in Figure 18, exhibit a smaller recirculation zone compared to the CFD results at the same time step (see Figure 15). In the SAM simulation, a strong thermal stratification layer forms near the top of the cavity. This stratification layer appears to be stronger than the momentum of the incoming colder fluid. As a result, the incoming flow is unable to break this barrier to create a recirculation region across the whole cavity. However, later in the transient ($t > 10$ min), this barrier is broken and flow recirculation occurs throughout the cavity, bringing down the temperature at the top region of the cavity. Moreover, noting that the top of the cavity is at $\tilde{y} = 2$, and that the highest temperature probe is at $\tilde{y} = 1.95$, this region is a small section of the cavity. As a result, the large overprediction of the temperature at this location does not have a significant influence on the outlet temperature.

Thus, by incorporating the turbulent viscosity from CFD simulations into the SAM model, a significant improvement in the prediction of the flow field is obtained. An additional outcome of this approach is that the temperature time series no longer exhibit large fluctuations as seen in the zero-equation model results (Figure 13). Owing to these improvements, we also use this modeling approach for the steady-state validation cases.

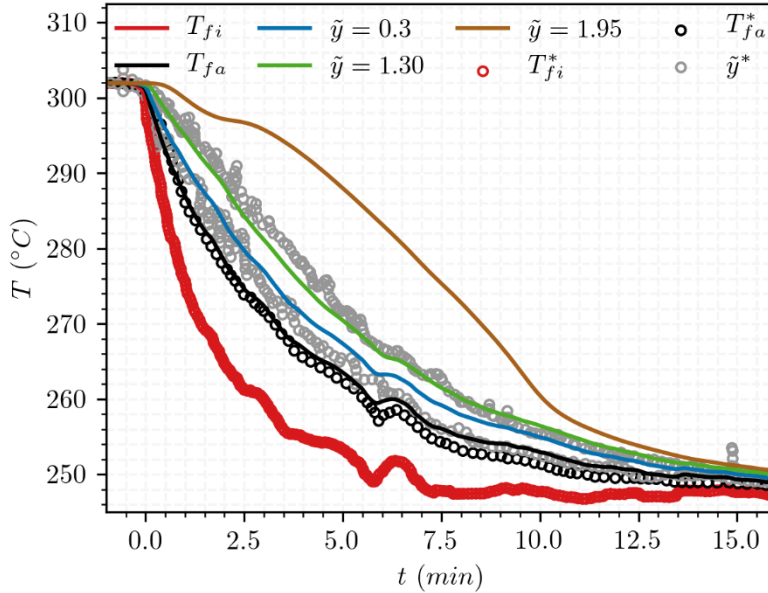


Figure 17: SAM results for case T1: Temperature time series at the inlet T_{fi} , outlet T_{fa} , and several \tilde{y} locations (along V2). The circles and solid lines represent the experimental data and the SAM results, respectively. Note that T_{fi} is overlapping with T_{fi}^* .

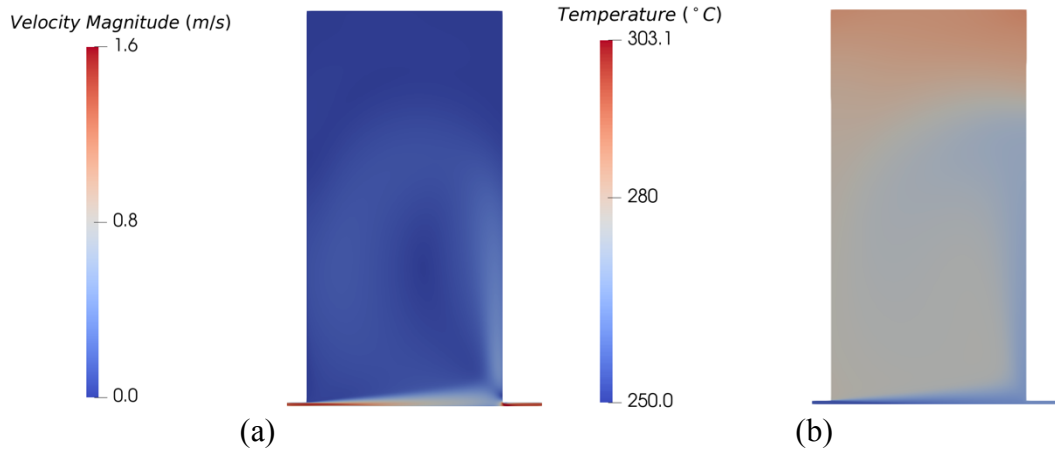


Figure 18: SAM results for case T1 at $t = 5$ min: a) Velocity distribution; b) temperature distribution.

4.3.2 Steady-state cases P3 and P4

Figure 19 shows the steady-state turbulent-viscosity distributions from the STAR-CCM+ CFD simulations for cases P3 and P4, which were performed with a mesh of 144,000 cells, and each simulation took approximately 30 core hours. The turbulent-viscosity data were extracted and used as input files for the SAM simulations. On a mesh with 31,000 cells, the SAM simulations execute in approximately 33 core-hours, comparable to the CFD cost. These turbulent-viscosity distributions exhibit strong mixing regions (dark red regions) at different locations, and indicate the location of the recirculation areas.

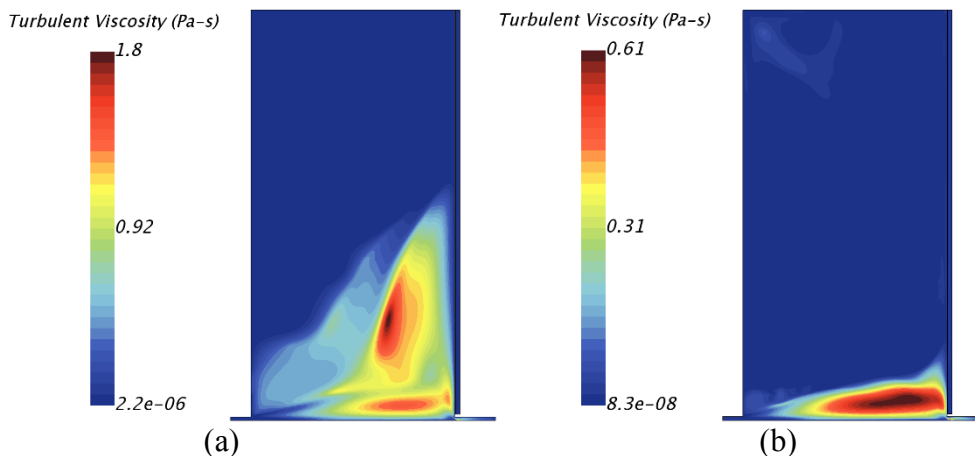


Figure 19: CFD results: Turbulent-viscosity distributions for cases a) P3; b) P4.

As observed in other simulations that make use of meshes, it is important to perform a mesh dependency study of the SAM simulations. To evaluate the mesh dependence in this modeling approach, a mesh-convergence analysis was carried out for case P4. A mesh-convergence plot of the temperature profile at location V2 is shown in Figure 20. In this plot, the solid line represents the results from CFD and the circles are the experimental data. Additionally, the dashed lines represent the SAM results, where the opacity of the dashed lines increases with increasing numbers of mesh elements. Here, we demonstrate that as the mesh is refined, the SAM model better predicts the rate of mixing, and therefore, the location of the thermal stratification layer. In this case, the CFD and SAM simulations overpredict the maximum temperature in the upper region of the cavity; however, a generally good prediction of the axial temperature distribution is obtained for both cases. Judging from this plot, a very coarse mesh could be used to obtain a general idea of the flow field; however, a finer mesh is required for better accuracy with the current model implementation. As a result, we proceeded using the most refined mesh for the simulations discussed in the remainder of this report.

The SAM simulation results for cases P3 and P4 are provided in Figure 21 and Figure 22, respectively. In these figures, the velocity magnitude and the temperature distributions are provided. Note that only the temperature distributions of the two cases have the same range. In these cases, thermally stratified layers are formed in the upper region of the cavity, thus indicating strong buoyancy effects created by the temperature gradients from the heating channel. While in both cases the jets have a tendency to travel upwards in the cavity when approaching the right wall, there is a strong thermal barrier which inhibits further penetration into the upper cavity. On the basis of the velocity and temperature distributions for both cases,

it is clear that the jet spread, and therefore the recirculation region, is larger in case P3, the case with the highest Reynolds number and lowest Richardson number (based on the values from Table 4).

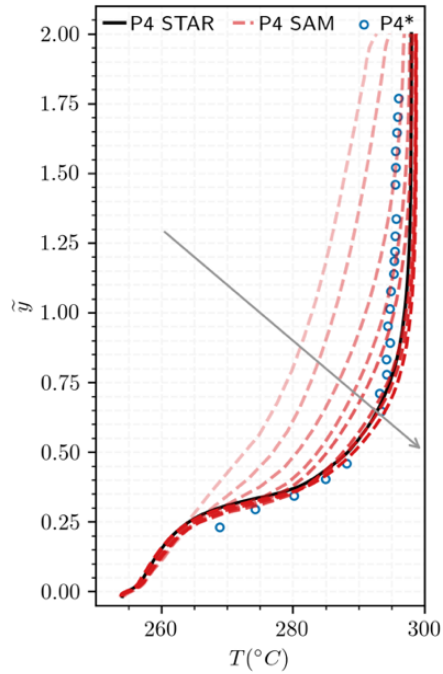


Figure 20: Mesh dependence of the SAM simulations. The arrow points in the direction of increasing number of elements.

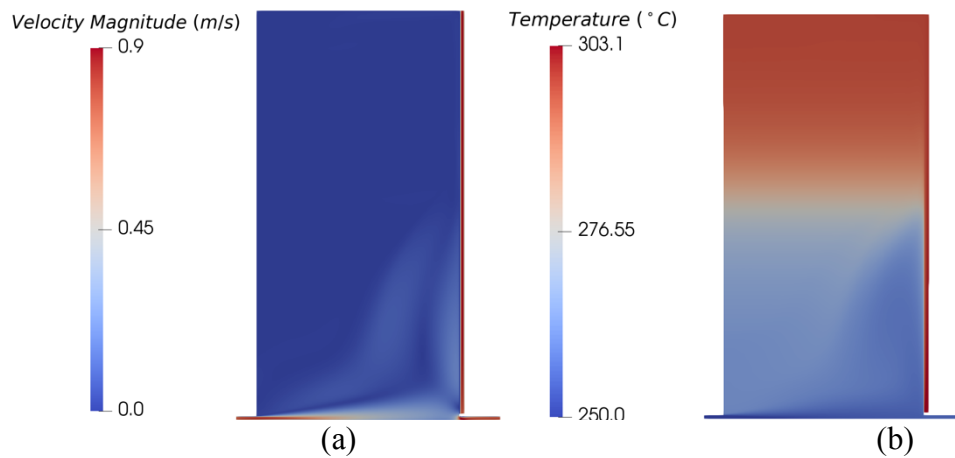


Figure 21: SAM results for case P3: a) Velocity distribution and b) temperature distribution.

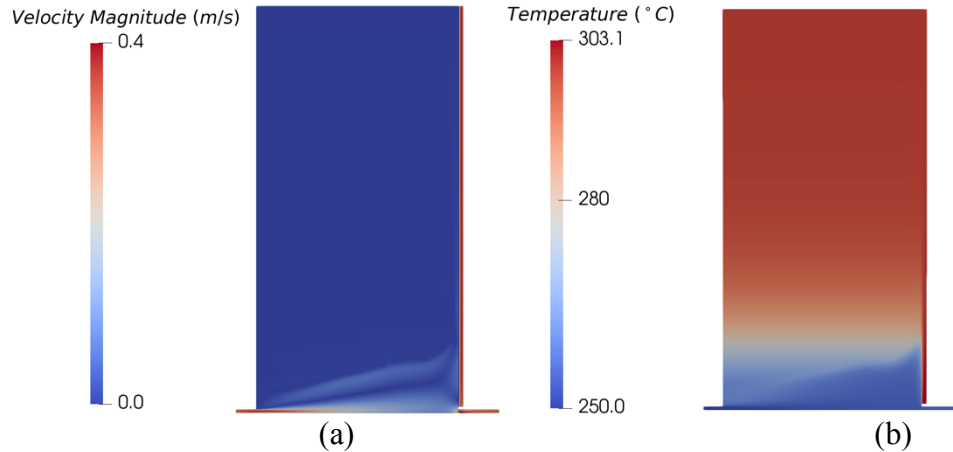


Figure 22: SAM results for case P4: a) Velocity distribution and b) temperature distribution.

A comparison for cases P3 and P4 between the CFD, SAM, and experimental temperature profiles at locations V1 and V2 is given in Figure 23. The simulations and experimental results indicate good agreement in both cases. The SAM model (results shown as dashed lines) is able to predict the temperature profiles along the height of the cavity as well as the CFD simulation for case P4. However, for case P3, some larger differences arise. In both cases, the largest differences occur past the thermal stratification layers, while the flow in the lower side of the cavity is well predicted. The SAM profiles differ by up to 3°C from the experimental data for case P4, while they differ by up to 4°C for case P3. Furthermore, as indicated by these profiles and the temperature distribution fields, the temperatures along the horizontal direction are roughly constant at different vertical locations after passing the recirculation region. This behavior indicates the presence of strong thermal stratification layers, which is well captured by the SAM simulations.

The comparisons between the SAM simulation results and the experimental data, provided in Figure 17 and Figure 23, provide a good basis for the validation of SAM's multi-dimensional flow model to predict flow recirculation and thermal stratification for high-Reynolds-number flows. While the zero-equation model was not able to predict the flow fields of interest, it provided a general basis for expansion to simulations with more information about the turbulence fields.

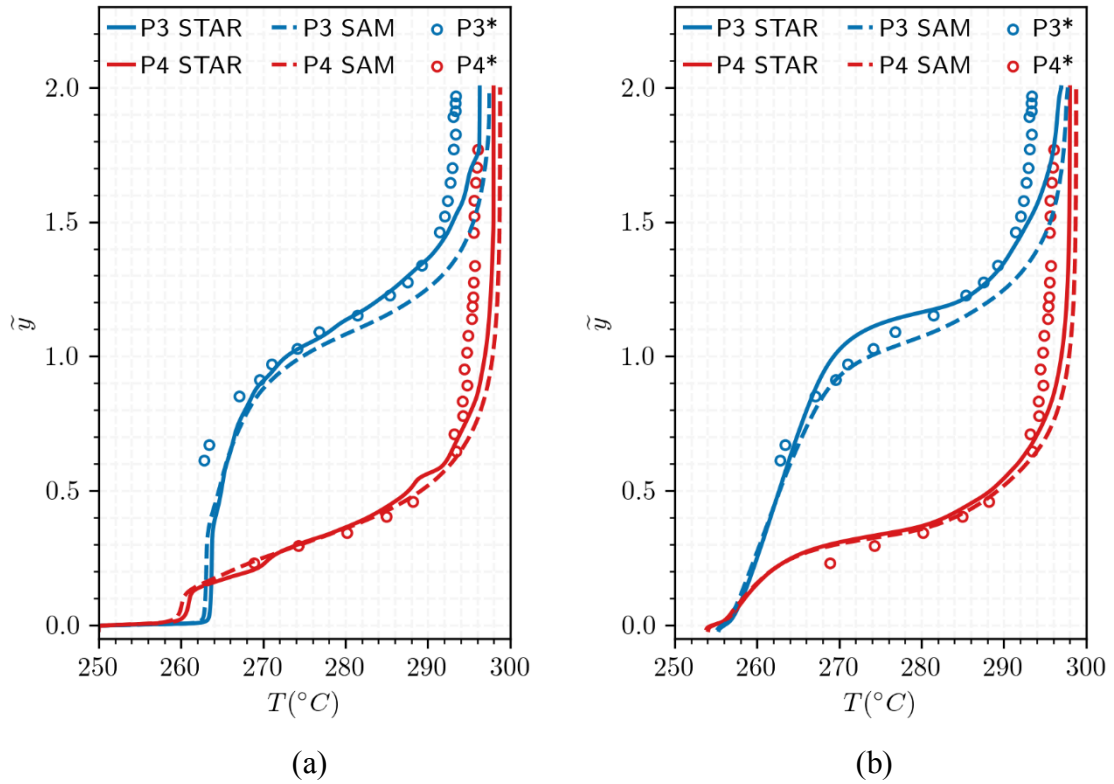


Figure 23: CFD, SAM, and experimental temperature profiles for cases P3 and P4 at locations a) V1 and b) V2. The circles and solid lines represent the experimental data and the CFD results, respectively. The dashed lines represent the SAM results.

5 Conclusions

Thermal mixing and stratification in large enclosures are very important phenomena critical to nuclear reactor safety. Owing to the wide ranges of time and length scales associated with such phenomena, accurate modeling and simulation of thermal mixing and stratification remain as the key unresolved and challenging problems for reactor transient analysis. Depending on simulation accuracy and computational resources, there exists a rich selection of modeling and simulation strategies that spans from highly simplified 0-D models to the complex high-resolution multi-dimensional CFD models. The 0-D models tend to be less computationally expensive; however, they can only deliver limited accuracies. On the other hand, high-resolution multi-dimensional CFD models are much more reliable in terms of prediction accuracy, but they are computationally expensive for whole-system transient analysis. When thermal mixing and stratification phenomena are of concern in system-level analysis, traditional system analysis codes tend to utilize the highly simplified 0-D models. As a result, it is desirable to have advanced and efficient thermal mixing and stratification modeling capabilities embedded in a system analysis code to improve the accuracy of reactor safety analyses.

SAM implemented a 0-D mixing model and a 1-D axial mixing model to address the modeling and simulation needs for the study of thermal mixing and stratification phenomena. Although both models have demonstrated acceptable modeling accuracy, their applications to more general and complex conditions could be questionable. The work presented in this report represents the latest SAM code capability enhancement, which introduces an improved multi-dimensional flow model into the code. It is well understood that turbulence modeling is of paramount importance for accurately capturing the potentially very complex flow fields. The current SAM code enhancements allow for two options to model the turbulent viscosity: (1) a zero-equation model based on the mixing length theory; and (2) importation from external sources (such as high-resolution CFD simulation results).

Additional code validation studies have been carried out using the experimental data from the SUPERCAVNA facility, including one transient and two steady-state test cases. Although the geometry of the SUPERCAVNA facility is quite simple, the flow conditions are indeed complex, and pose great challenges for numerical simulations because of the very different length scales in the test facility. The SAM code validation study started with the use of the highly simplified zero-equation turbulence model, and it was determined that this model is too simple to capture the complex flow and thermal mixing behaviors. Subsequently, the code validation continued with the use of turbulent viscosity data from high-resolution STAR-CCM+ CFD simulations to improve the accuracy of the results. Using this approach, the SAM simulation results showed very good agreement with both the SUPERCAVNA experimental data and STAR-CCM+ simulation results.

This work presents an attempt to include a built-in advanced multi-dimensional flow model in a system analysis code to overcome the simulation challenges of thermal mixing and stratification. This new code capability has been successfully validated against the very complex SUPERCAVNA transient and steady-state experimental data. This result shows that the SAM code has a very high potential to effectively treat the thermal mixing and stratification phenomena that pose significant challenges to traditional system analysis codes. However, further research will be needed to further improve the code's capabilities, such as a more efficient and robust approach to capture turbulence effects. As discussed in the introduction section, a separate Argonne LDRD project is investigating a data-driven turbulence model

approach, and we hope that this separate study will shed some light on turbulence modeling in the coming machine-learning era and inform our plan to implement the machine-learning-based turbulence model in SAM.

Acknowledgment

This work is supported by the U.S. DOE Office of Nuclear Energy's Nuclear Energy Advanced Modeling and Simulation program. The submitted manuscript has been created by UChicago Argonne, LLC, Operator of Argonne National Laboratory ("Argonne"). Argonne, a U.S. Department of Energy Office of Science laboratory, is operated under Contract No. DE-AC02-06CH11357.

References

- [1] S. Moriya, N. Takana, N. Katano, and A. Wada. Effects of Reynolds Number and Richardson Number on Thermal Stratification in Hot Plenum. *Nuclear Engineering and Design*, 99:441–451, 1987.
- [2] Y. Ieda, I. Maekawa, T. Muramatsu, and S. Nakanishi. Experimental and analytical studies of the thermal stratification phenomenon in the outlet plenum of fast breeder reactors. *Nuclear Engineering and Design*, 120:403–414, 1990.
- [3] O. Auban, R. Zboray, and D. Paladino. Investigation of large-scale gas mixing and stratification phenomena related to LWR containment studies in the PANDA facility. *Nuclear Engineering and Design*, 237(4):409–419, 2007.
- [4] M. Andreani, A. Badillo, and R. Kapulla. Synthesis of the OECD/NEA-PSI CFD benchmark exercise. *Nuclear Engineering and Design*, 299:59–80, 2016.
- [5] B. Ward, J. Clark, and H. Bindra. Thermal stratification in liquid metal pools under influence of penetrating colder jets. *Experimental Thermal and Fluid Science*, 103:118–125, 2019.
- [6] J. Schneider, M. Anderson, E. Baglietto, L. Xu, Z. Wu, S. Morgan, M. Bucknor, M. Weathered, and S. Bilbao y Leon. Thermal stratification in a pool-type geometry. In *Proceedings of the 18th International Topical Meeting on Nuclear Reactor Thermal Hydraulics (NURETH-18)*, Portland, USA, 2019.
- [7] H. Zhao and P. F. Peterson. An Overview of Modeling Methods for Thermal Mixing and Stratification in Large Enclosures for Reactor Safety Analysis. In *Proceedings of the 8th International Topic Meeting on Nuclear Thermal-Hydraulics, Operation and Safety (NUTHOS-8)*, Shanghai, China, 2010.
- [8] T. H. Fanning. The SAS4A/SASSYS-1 Safety Analysis Code System. Technical report, ANL/NE-12/4, Argonne National Laboratory, 2012.
- [9] The RELAP5-3D Code Development Team. RELAP5-3D Code Manual Volume I: Code Structure, Systems Models, and Solution Methods. Technical report, INEEL-EXT-98-00834 Rev. 2.0, Idaho National Laboratory, 2002.
- [10] M. Robert, M. Farvacque, M. Parent, and B. Faydide. CATHARE 2 V2.5: A Fully Validated CATHARE Version for Various Applications. In *Proceedings of the 10th International Topical Meeting on Nuclear Reactor Thermal Hydraulics (NURETH-10)*, Seoul, Republic of Korea, 2003.
- [11] U.S. Nuclear Regulatory Commission. MELCOR Computer Code Manuals, Technical report, NUREG/CR-6119, Vol. 2, Rev. 3, SAND 2005-5713, 2005.
- [12] P.F. Peterson. Scaling and analysis of mixing in large stratified volumes. *International Journal of Heat and Mass Transfer*, 37:97–106, 1994.
- [13] P. F. Peterson and R. Gamble. Scaling for forced-convection augmentation of heat and mass transfer in large enclosures by injected jets. *Transactions of the American Nuclear Society*, 78:265–266, 1998.
- [14] H. Zhao. Computation of Mixing in Large Stably Stratified Enclosures. PhD thesis, University of California, Berkeley, 2003.

- [15] S. Kuhn, H. K. Kang, and P. F. Peterson. Study of Mixing and Augmentation of Natural Convection Heat Transfer by a Forced Jet in a Large Enclosure. *Journal of Heat Transfer*, 124(4):660–666, 2002.
- [16] H. Zhao, L. Zou, and H. Zhang. Simulation of thermal stratification in BWR suppression pools with one dimensional modeling method. *Annals of Nuclear Energy*, 63:533–540, 2014.
- [17] G. Wilson and H. Bindra. Thermal Stratification and Mixing in SFR Plena Using a One-Dimensional Scalar Transport Model. In *Advances in Thermal Hydraulics 2018 (ATH 2018)*, Orlando, Florida, 2018.
- [18] C. Lu, Z. Wu, S. Morgan, J. Schneider, M. Anderson, L. Xu, E. Baglietto, M. Bucknor, M. Weathered, and S. Bilbao y Leon. An Efficient 1-D Thermal Stratification Model for Pool-Type Sodium-Cooled Fast Reactors. *Nuclear Technology*, published online Mar. 2, 2020.
- [19] A. Kraus and R. Hu. CFD analysis of upper plenum flow for a sodium-cooled small modular reactor. In *Proceedings of the 16th International Topical Meeting on Nuclear Reactor Thermal Hydraulics (NURETH-16)*, Chicago, Illinois, 2015, pages 6625–6638.
- [20] T. H. Fanning and J. W. Thomas. Integration of CFD into systems analysis codes for modeling thermal stratification during SFR transients. In *Proceedings of the 14th International Topical Meeting on Nuclear Reactor Thermal Hydraulics (NURETH-14)*, Toronto, ON, Canada, 2011.
- [21] R. Hu. SAM Theory Manual. Technical Report, ANL/NE-17/4, Argonne National Laboratory, 2017.
- [22] R. Hu. An advanced one-dimensional finite element model for incompressible thermally expandable flow. *Nuclear Technology*, 190(3):313–322, 2015.
- [23] R. Hu. A fully-implicit high-order system thermal-hydraulics model for advanced non-LWR safety analyses. *Annals of Nuclear Energy*, 101:174–181, 2017.
- [24] R. Hu and T. Sumner. Benchmark Simulations of the Thermal-Hydraulic Responses during EBR-II Inherent Safety Tests using SAM. In *2016 International Congress on Advances in Nuclear Power Plants (ICAPP 2016)*, San Francisco, California, 2016.
- [25] R. Hu, Y. Zhu, and A. Kraus. Advanced Model Developments in SAM for Thermal Stratification Analysis during Reactor Transients. Technical report, ANL/NSE-18/7, Argonne National Laboratory, 2018.
- [26] R. Hu. Three-dimensional flow model development for thermal mixing and stratification modeling in reactor system transients analyses. *Nuclear Engineering and Design*, 345:209–215, 2019.
- [27] G. K. Batchelor. *An Introduction to Fluid Dynamics*. Cambridge University Press, 1967.
- [28] D. A. Yoder. Comparison of Turbulent Thermal Diffusivity and Scalar Variance Models. In *Proceedings of the 54th AIAA Aerospace Sciences Meeting*, p. 1561, 2016.
- [29] G. Iaccarino. Simulation of Turbulent Flows. <https://web.stanford.edu/class/me469b/handouts/turbulence.pdf>, 2004. Accessed: 2020-06-09.
- [30] G. Alfonsi. Reynolds-averaged Navier-Stokes equations for turbulence modeling. *Applied Mechanics Reviews*, 62(4):040802, 2009.

- [31] D. A. Nield and A. Bejan. Convection in Porous Media, fourth edition. Springer, 2013.
- [32] M. Kaviany. Principles of Heat Transfer in Porous Media, second edition. Springer, 1995.
- [33] H. K. Versteeg and W. Malalasekera. An Introduction to Computational Fluid Dynamics: The Finite Volume Method, second edition. Springer, 2013.
- [34] D. F. Griffiths. The ‘No Boundary Condition’ Outflow Boundary Condition. International Journal for Numerical Methods in Fluids, 24(4):393–411, 1997.
- [35] L. Halpern. Artificial Boundary Conditions for the Linear Advection Diffusion Equation. Mathematics of Computation, 46(174):425–438, 1986.
- [36] R. Verfurth. Finite element approximation on incompressible Navier-Stokes equations with slip boundary condition. Numerische Mathematik, 50(6):697–721, 1986.
- [37] R. Verfurth. Finite element approximation of incompressible Navier-Stokes equations with slip boundary condition ii. Numerische Mathematik, 59(1):615–636, 1991.
- [38] P. B. Mucha. On Navier–Stokes equations with slip boundary conditions in an infinite pipe. Acta Applicandae Mathematica, 76(1):1–15, 2003.
- [39] R. Vidil, D. Grand, and F. Leroux. Interaction of recirculation and stable stratification in a rectangular cavity filled with sodium. Nuclear Engineering and Design, 105(3):321–332, 1988.
- [40] R. Vidil, R. Martin, and R. Grand. Mixed convection of liquid metal in a rectangular cavity. In Proceedings of the International Topical Meeting on Nuclear Reactor Thermal Hydraulics (NURETH), 1983.
- [41] E. A. Griffiths and E. Griffiths. The Coefficient of Expansion of Sodium. Proceedings of the Physical Society of London, 27(1):477–484, 1914. ISSN 14697793.
- [42] A. Ribes and C. Caremoli, Salomé platform component model for numerical simulation, COMPSAC 07: Proceeding of the 31st Annual International Computer Software and Applications Conference, pages 553-564, Washington, DC, USA, 2007, IEEE Computer Society.
- [43] Siemens, STAR-CCM+ 12.06 Documentation, 2017.



Nuclear Science and Engineering Division

Argonne National Laboratory
9700 South Cass Avenue, Bldg. 208
Argonne, IL 60439

www.anl.gov



Argonne National Laboratory is a U.S. Department of Energy
laboratory managed by UChicago Argonne, LLC